120

ORNL-3690
UC-80 – Reactor Technology
TID-4500 (37th ed.)

PHOTOELASTIC ANALYSIS OF EGCR PRESSURE VESSEL

J. E. Smith
C. C. Wilson
W. F. Swinson

OAK RIDGE NATIONAL LABORATORY
operated by
UNION CARBIDE CORPORATION
for the
U.S. ATOMIC ENERGY COMMISSION

Printed in USA. Price $2.00. Available from the Clearinghouse for Federal Scientific and Technical Information, National Bureau of Standards, U.S. Department of Commerce, Springfield, Virginia

ORNL-3690

Contract No. W-7405-eng-26

Reactor Division

PHOTOELASTIC ANALYSIS OF EGCR PRESSURE VESSEL

J. E. Smith
Oak Ridge National Laboratory

C. C. Wilson
University of Tennessee

W. F. Swinson
Auburn University

FEBRUARY 1965

OAK RIDGE NATIONAL LABORATORY
Oak Ridge, Tennessee
operated by
UNION CARBIDE CORPORATION
for the
U.S. ATOMIC ENERGY COMMISSION

CONTENTS

List of Figures

PHOTOELASTIC ANALYSIS OF EGCR PRESSURE VESSEL

J. E. Smith C. C. Wilson
W. F. Swinson

Abstract

A three-dimensional photoelastic stress analysis of the top head of the Experimental Gas-Cooled Reactor (EGCR) pressure vessel was made to amplify and augment information obtained from a study of a strain-gaged model and to provide additional information regarding the stresses and stress distributions. The results verified the adequacy of the structural design and, in general, agreed with the results of the strain-gage analysis.

The photoelastic model had a scale factor of 1/14.2 and was fabricated from Bakelite ERL-2774 epoxy resin. The fabrication procedures, the methods for loading, and the procedure for freezing stresses in the model are described. Both internal pressure and an axial load were imposed on one nozzle. Procedures used for data collection and reduction are discussed.

The stress distributions given are for the spherical head in regions between the cluster nozzles and adjacent to the gas-outlet and burst-slug-detection nozzles. Stresses in the cylindrical portion of the pressure vessel and in the transition region between the head and shell are also given. The only nozzle stresses shown are for the gas-outlet and burst-slug-detection nozzles. All stress distributions are presented graphically.

The isoclinic lines in the nozzle-to-shell attachment region for a nonradially attached (hillside) nozzle were obtained. A comprehensive discussion of all results is given, along with a description of the methods used in correcting for data distortion due to surface effects.

1. Introduction

The pressure vessel for the Experimental Gas-Cooled Reactor[1] (EGCR) is a cylindrical shell having hemispherical top and bottom heads. The vessel has an overall height of 46 ft 4 in., an inside diameter of 20 ft,

---

[1]Experimental Gas-Cooled Reactor Final Hazards Summary Report, Vol. 1, USAEC Report ORO-586, Oct. 10, 1962.

and a minimum wall thickness of 2 3/4 in. (Fig. 1). The hemispherical heads are 4 in. thick. The entire vessel is constructed of carbon steel, type SA-212, grade B. The design pressure is 350 psig, and the design temperature is 650°F.

As shown in Fig. 1, the upper head of the pressure vessel has numerous nozzle penetrations that make this a crucial region from a structural standpoint. The large number of nozzles in close proximity makes an accurate theoretical analysis difficult, and the use of nozzles aligned vertically rather than normal to the shell adds to the complexity of any analytical study. Hence, experimental stress analyses of the pressure vessel were carried out using two separate models of the top head and adjacent cylindrical region. One was an aluminum model[2] for use in a strain-gage analysis, while the other was an epoxy-resin photoelastic model.

The structural adequacy of the design was established on the basis of the strain-gage analysis. The three-dimensional photoelastic analysis was made to amplify the information gained from the strain-gage analysis, to serve as a check on that analysis, and to give additional information concerning the stress concentrations at the junctions between the nozzles and the hemispherical head. In addition, it was possible to obtain detailed distributions in the spherical shell.

At the time the experimental program was initiated, there were 53 nozzles in the closely spaced cluster in the head, and the designs of the test vessels were based upon this number. Later, 12 special plug nozzles were eliminated. The nozzles removed are shown dotted in Fig. 2.

This report includes the results obtained from an examination of the head, the cylindrical shell, the gas-outlet nozzles, and the burst-slug-detection nozzles. The model is described; its history is cited; and the experimental procedures are discussed. The results are shown graphically, and, where possible, comparisons are made with the strain-gage results.

---

[2]B. L. Greenstreet et al., Experimental Stress Analysis of EGCR Pressure Vessel, USAEC Report ORNL-3157, Oak Ridge National Laboratory, Nov. 14, 1961.

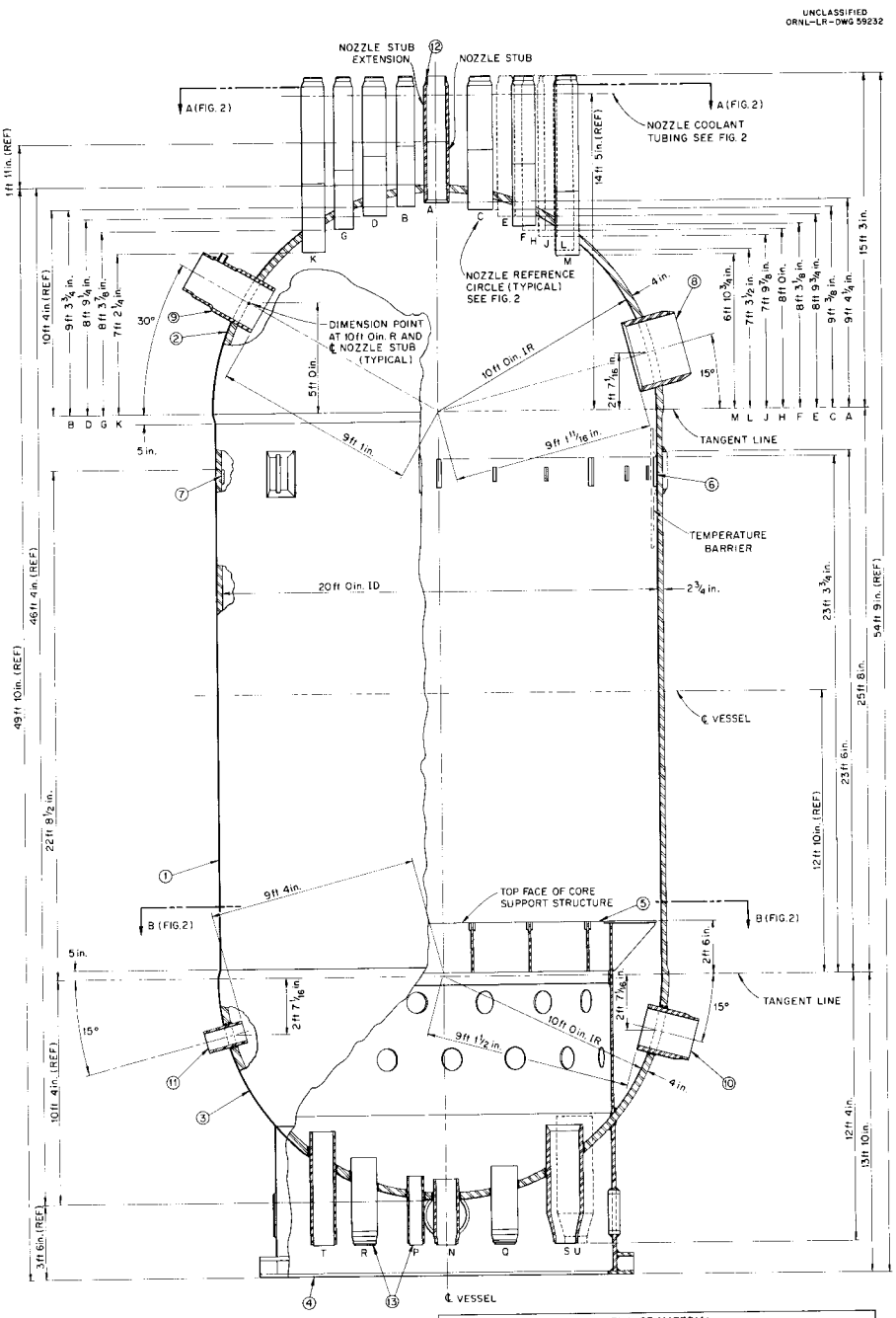

BILL OF MATERIAL

ITEM	REQ'D	DESCRIPTION	MATERIAL
1	1	PRESSURE VESSEL CYLINDER	SA 212 GRADE B
2	1	PRESSURE VESSEL TOP HEAD	SA 212 GRADE B
3	1	PRESSURE VESSEL BOTTOM HEAD	SA 212 GRADE B
4	1	VESSEL SUPPORT	
5	1	CORE SUPPORT STRUCTURE	
6	8	LATERAL RESTRAINT LUGS	
7	16	BARRIER SUPPORT LUG	
8	2	GAS OUTLET NOZZLE STUB	
9	2	B.S.D. AND TC NOZZLE STUB AND EXTENSION	
10	2	GAS INLET NOZZLE STUB	
11	4	THERMOCOUPLE NOZZLE STUB AND EXTENSION	
12	41	TOP HEAD NOZZLE STUBS AND EXTENSIONS	
13	29	BOTTOM HEAD NOZZLE STUBS	

Fig. 1. EGCR Pressure Vessel Elevation.

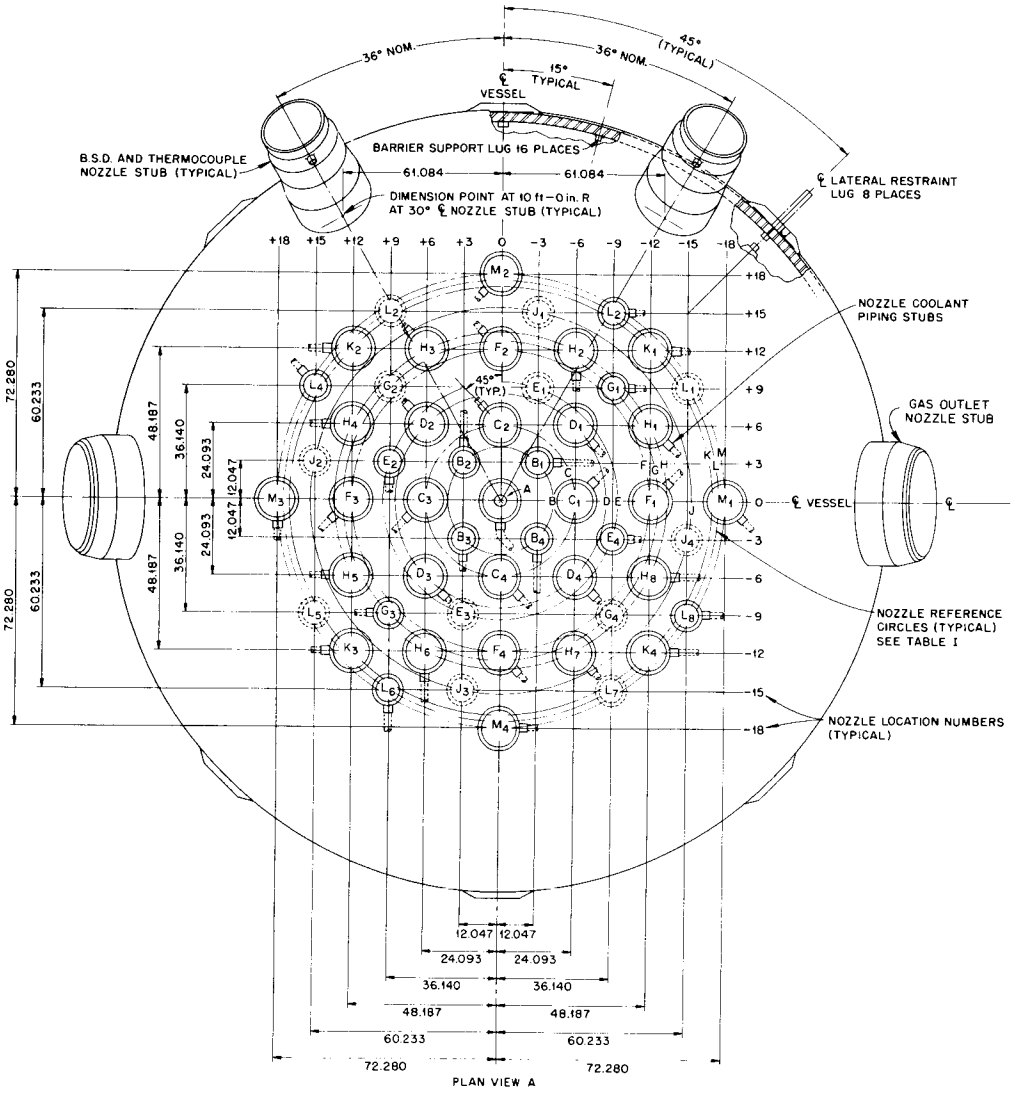

TABLE I

NOZZLE REF. CIRCLE	NOZZLE REF. CIRCLE R (REF. DIM. FOR ORIENTATION ONLY)	NOZZLE TYPE	REQ'D	REMARKS
A	0	CONTROL ROD	1	
B	17.037 in.	SMALL THRU-LOOP	4	
C	24.093 in.	CONTROL ROD	4	
D	34.073 in.	CONTROL ROD	4	
E	38.095 in.	SPECIAL PLUG	2	2 REMOVED
F	48.187 in.	CONTROL ROD	4	
G	51.110 in.	SPECIAL PLUG	2	2 REMOVED
H	53.875 in.	CONTROL ROD	8	
J	61.427 in.	SPECIAL PLUG		4 REMOVED
K	68.147 in.	LARGE THRU-LOOP	4	
L	70.244 in.	SPECIAL PLUG	4	4 REMOVED
M	72.280 in.	CONTROL ROD	4	

Fig. 2. EGCR Pressure Vessel Plan.

2. Description and History of Model

The dimensions and the slicing plan for the photoelastic model are shown in Figs. 3 and 4. The scale factor for the model was 1/14.2. The model was cast from Bakelite ERL-2774 epoxy resin, with phthalic anhydride and hexahydrophthalic anhydride as hardeners. The material was mixed in the following proportions:

	Quantity (lb)
Bakelite ERL-2774	1
Phthalic anhydride	0.45
Hexahydrophthalic anhydride	0.10

The head and shell were integrally cast and machined, while the nozzles and calibration bars were cast from the same batch of material and machined separately. The cement used for attaching the nozzles was Bakelite ERL-2774 epoxy resin with a room-temperature hardener, CIBA HN 951. Approximately 12 parts of hardener per 100 parts of resin were used. The finished model is shown in Fig. 5. The long nozzle is nozzle A (see Fig. 4 for location). This nozzle was made longer than the other cluster nozzles in order that the membrane stresses could be checked.

Before attaching the nozzles the model components were cured in the following sequence:

1. Heated at a rate of 3°F/hr to 320°F.
2. Cured for 10 days at 320°F.
3. Cooled at a rate of 3°F/hr to room temperature.

After the nozzles were attached, the model was mounted on a baseplate, which was separately cast of the same material, and rigged in the oven for loading. The model was subjected to an internal pressure of 1.28 psig (2.6 in. Hg) with an axial compressive load of 4.52 lb on nozzle M_3. When assessing the adequacy of the reactor vessel, these loads must be related to those applied to the prototype. The maximum design loads on the prototype are 350 psi internal pressure and an axial compressive load of 42,000 lb on nozzle M_3. The oven loading arrangement of the model and calibration bars is shown in Fig. 6.

UNCLASSIFIED
ORNL-DWG 64-9554

NOZZLE	INSIDE DIAMETER	OUTSIDE DIAMETER
A,C,D,F,H,K,M	0.7834 in.	0.9507 in.
B,E,G,J,L	0.5458 in.	0.6690 in.
GAS OUTLET	2.394 in.	2.661, 2.746 in.
BSD	1.549 in.	1.831 in.

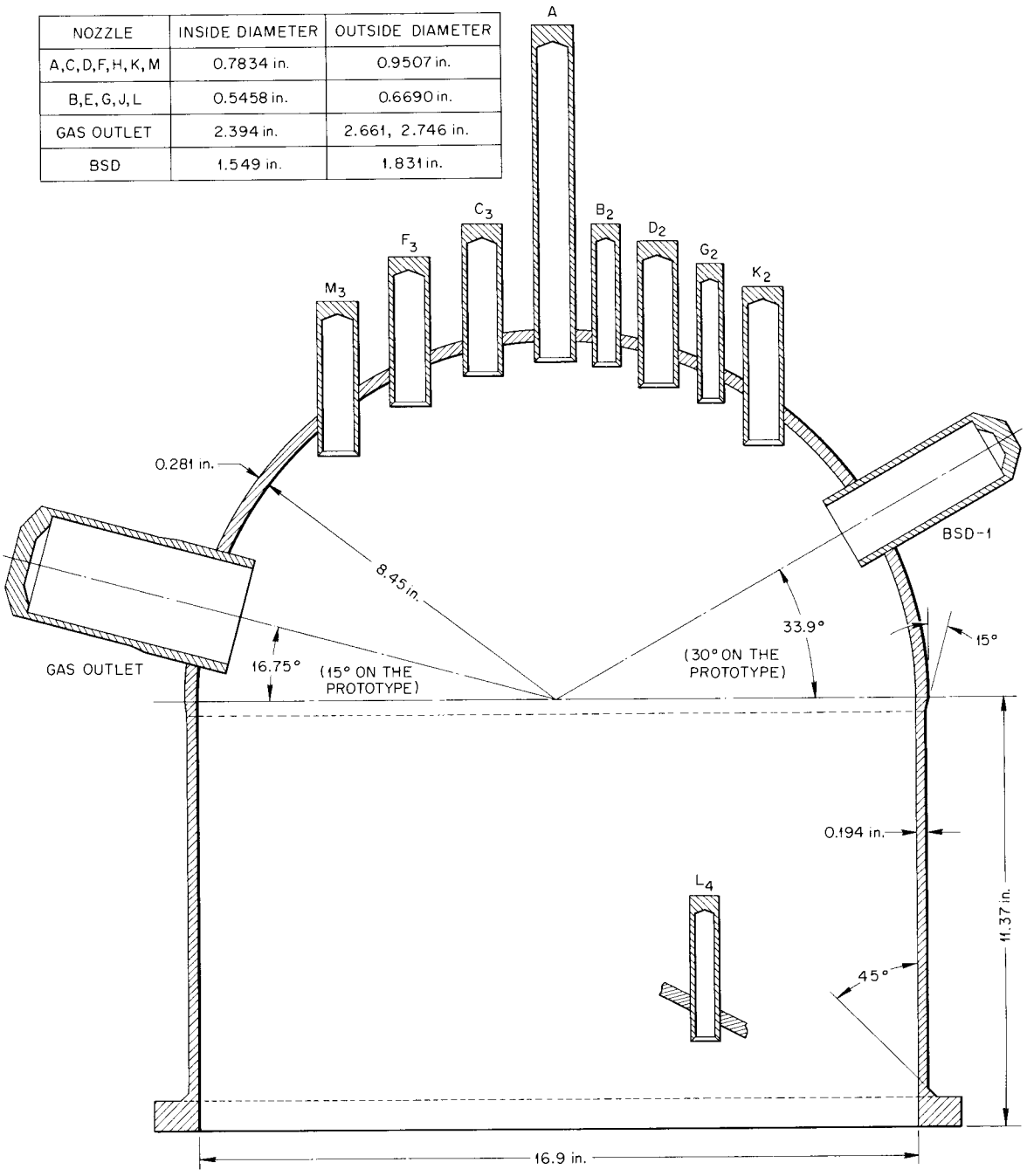

Fig. 3. EGCR Pressure Vessel Photoelastic Model Elevation Section A-A From Fig. 4.

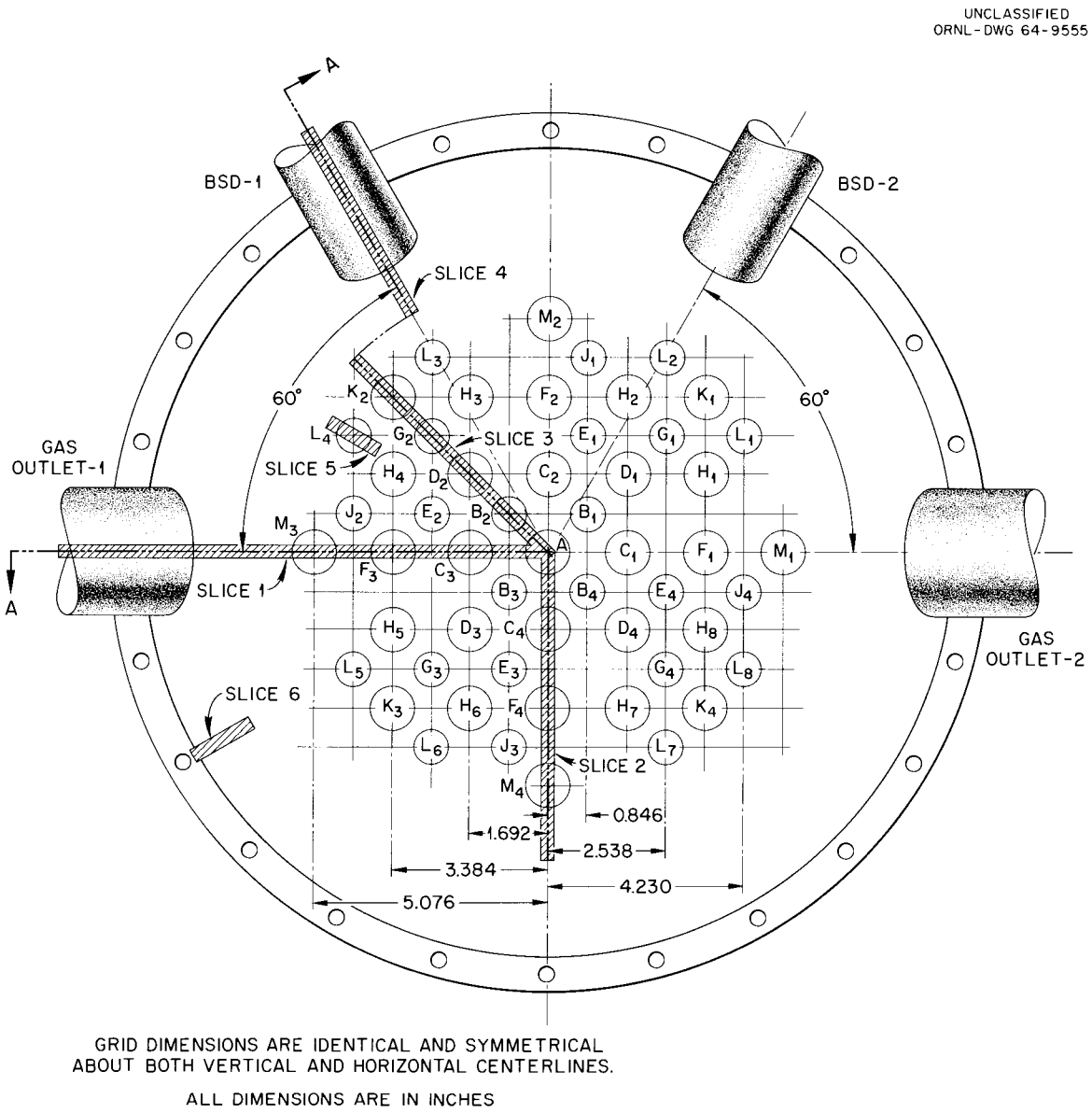

Fig. 4. EGCR Pressure Vessel Photoelastic Model Plan.

The procedure for freezing stresses in the model was the following:

1. Heat at a rate of 7 1/2°F/hr to 300°F.
2. Hold at 300°F for 2 hr.
3. Apply loads.
4. Hold in loaded state at 300°F for 15 min.
5. Cool in loaded state at a rate of 3 3/4°F/hr to room temperature.

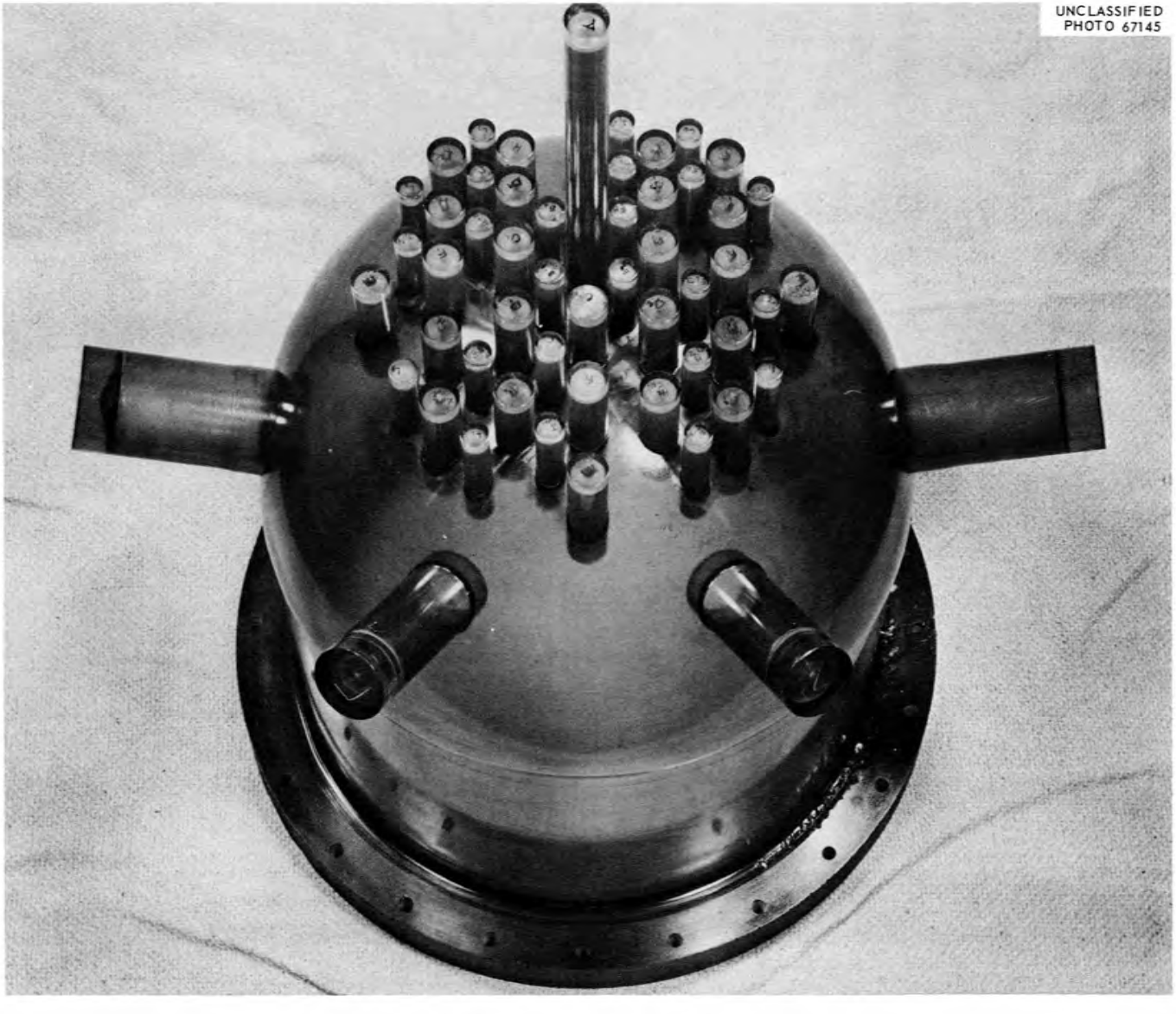

Fig. 5. Oblique View of Finished Model.

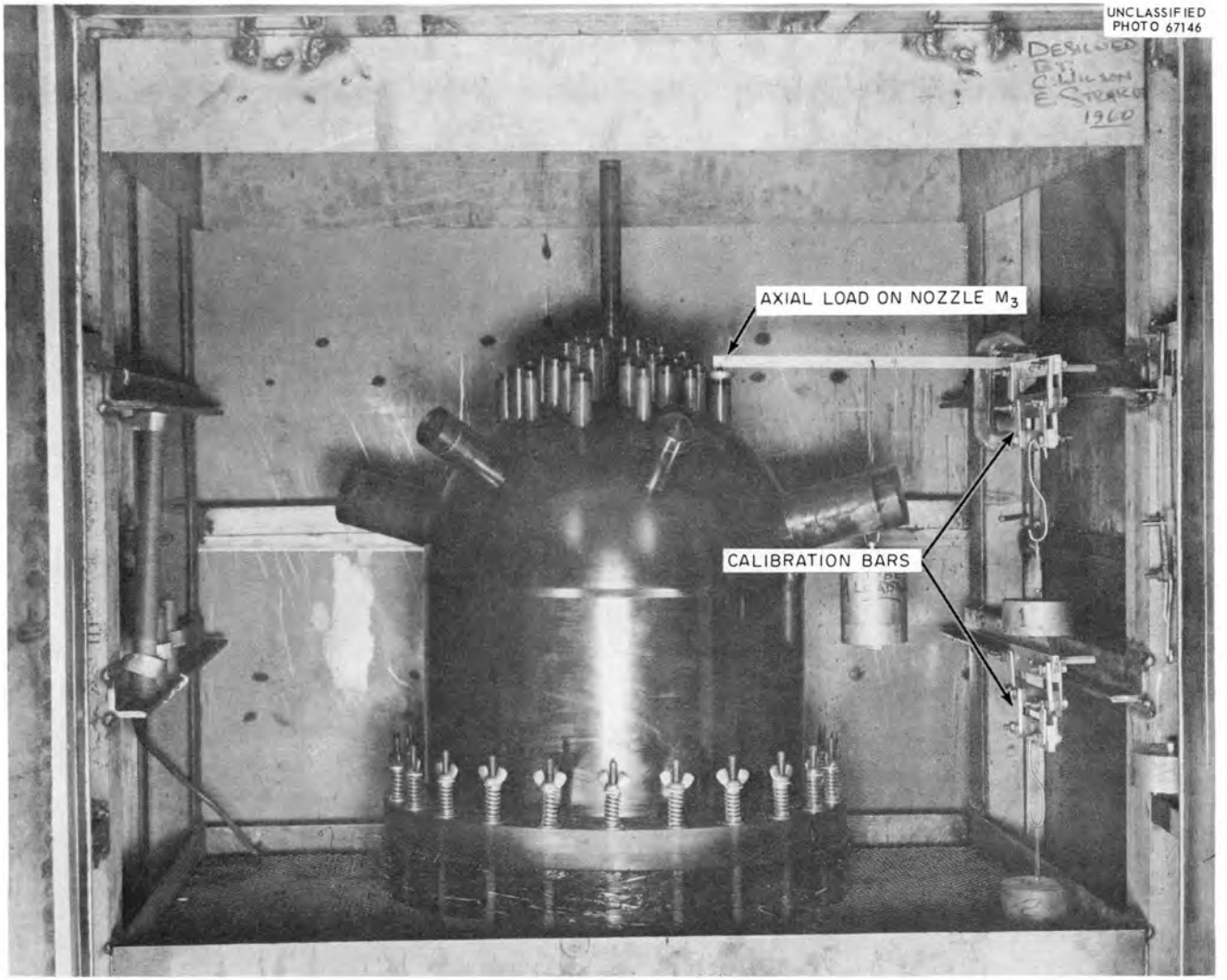

Fig. 6. Oven Arrangement Showing Model Subjected to an Internal Pressure of 1.28 psi With an Axial Compressive Load of 4.52 lb on Nozzle M_3.

Actually, the rate of rise in temperature was observed to be slightly less than the programmed 7 1/2°F/hr.

It may be noted from Fig. 3 that the angular positions of the burst-slug-detection and gas-outlet nozzles, as measured after fabrication, differ slightly from those on the prototype. The effects of these differences were considered to be negligible.

3. Experimental Procedure and Data Reduction

Analyses of surface stresses were made in the same regions of the vessel as those studied in the strain-gage analysis. Stresses in the circumferential and axial or meridional directions were examined in the slices taken from the model as shown in Fig. 4.

To obtain the desired slices, the nozzle cluster was cut from the rest of the model and cast in Duroc dental plaster. (This procedure was pretested on samples of the photoelastic material to ensure that no change in the pattern of the frozen fringes would occur.) Slices were then rough cut from the cluster region with a band saw and recast in plaster for finish machining with a fly cutter. The axial and meridional slices had a final thickness of 0.125 in., with a tolerance of ±0.002 in. A section of the sliced nozzle cluster is shown in Fig. 7. Typical slices are shown in Figs. 8 and 9, and the calibration bars are shown in Fig. 10.

The Coker compensator method[3] was used to determine the differences in the principal stresses ($p - q$ values) at the surface. Using white light, a calibrated tensile specimen was placed between the light source and the slice with frozen stresses. With polarized light passing through both specimens, a dark zone was formed when the fringe order of the calibrated compensator bar equaled the fringe order of the model at the point of extinction. Therefore,

$$(p - q)_m = \sigma_c \frac{C_c t_c}{C_m t_m} ,$$

[3]M. M. Frocht, Photoelasticity, Vol. II, pp. 382–383, Wiley, New York, 1948.

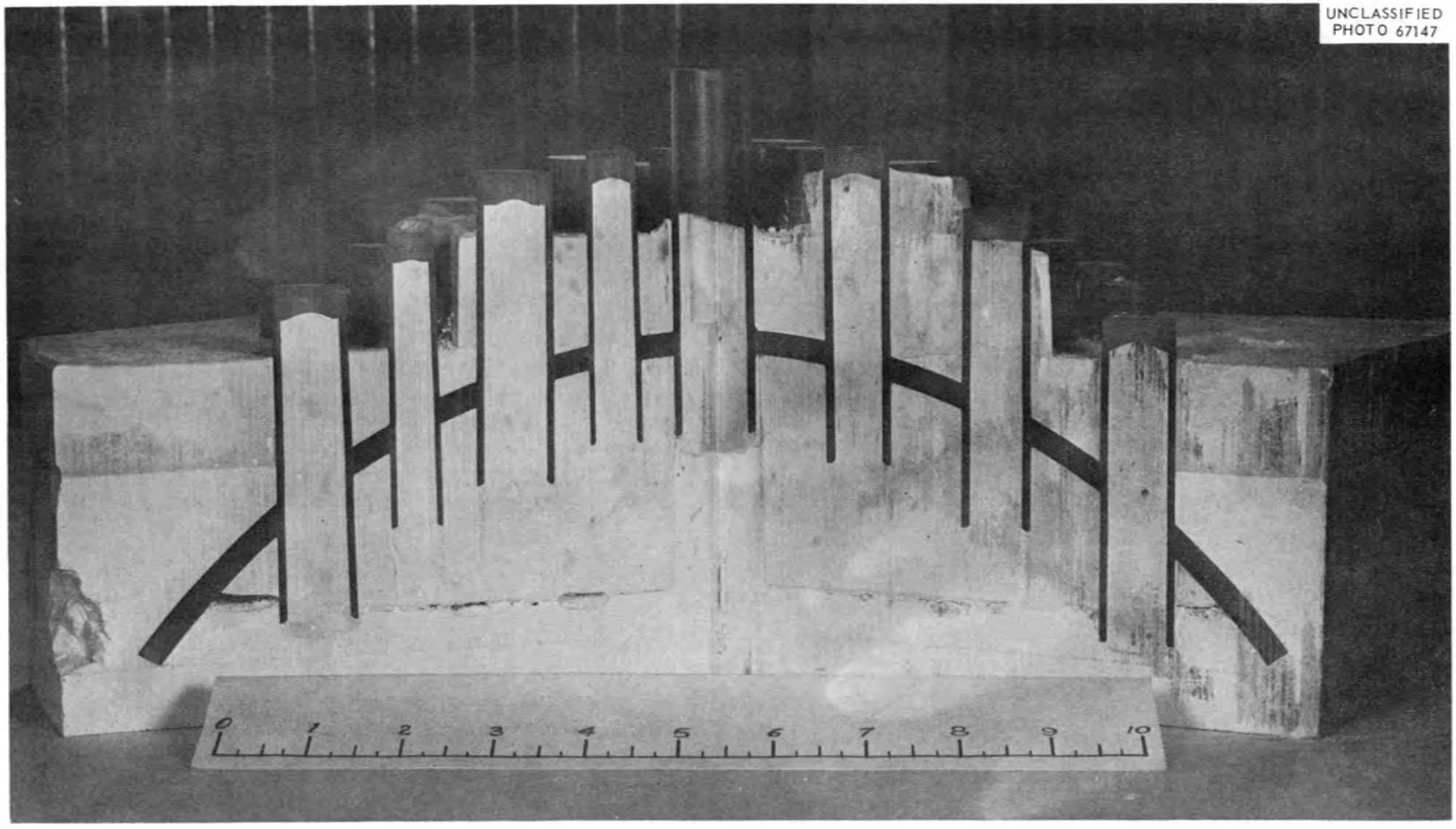

Fig. 7. Nozzle Cluster Showing Slices 2 and 3.

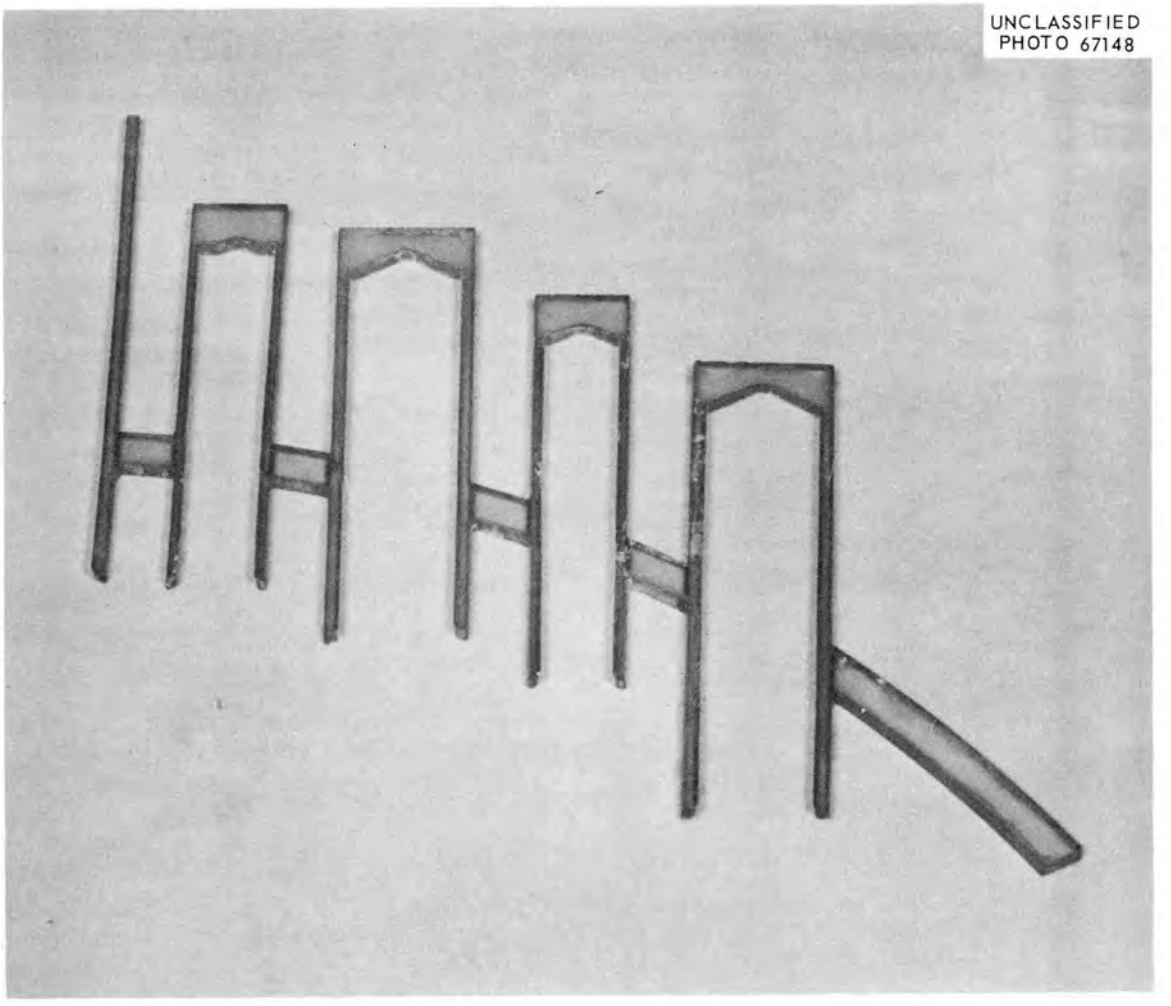

Fig. 8. Slice 3 Through Nozzle Cluster.

where

$(p - q)_m$ = principal stress difference in the model,

σ_c = tensile stress in compensator,

C_c = compensator stress-optic constant, ratio of wave length λ_c to fringe factor f_c,

C_m = model stress-optic constant, λ_m/f_m,

t_m = thickness of the model,

t_c = thickness of the compensator.

Since one of the principal stresses was known at the surface, the other principal stress could be determined by compensation. For a positive principal stress difference, complete extinction occurs when the tensile compensator is placed perpendicular to the free boundary. If $p - q$ is

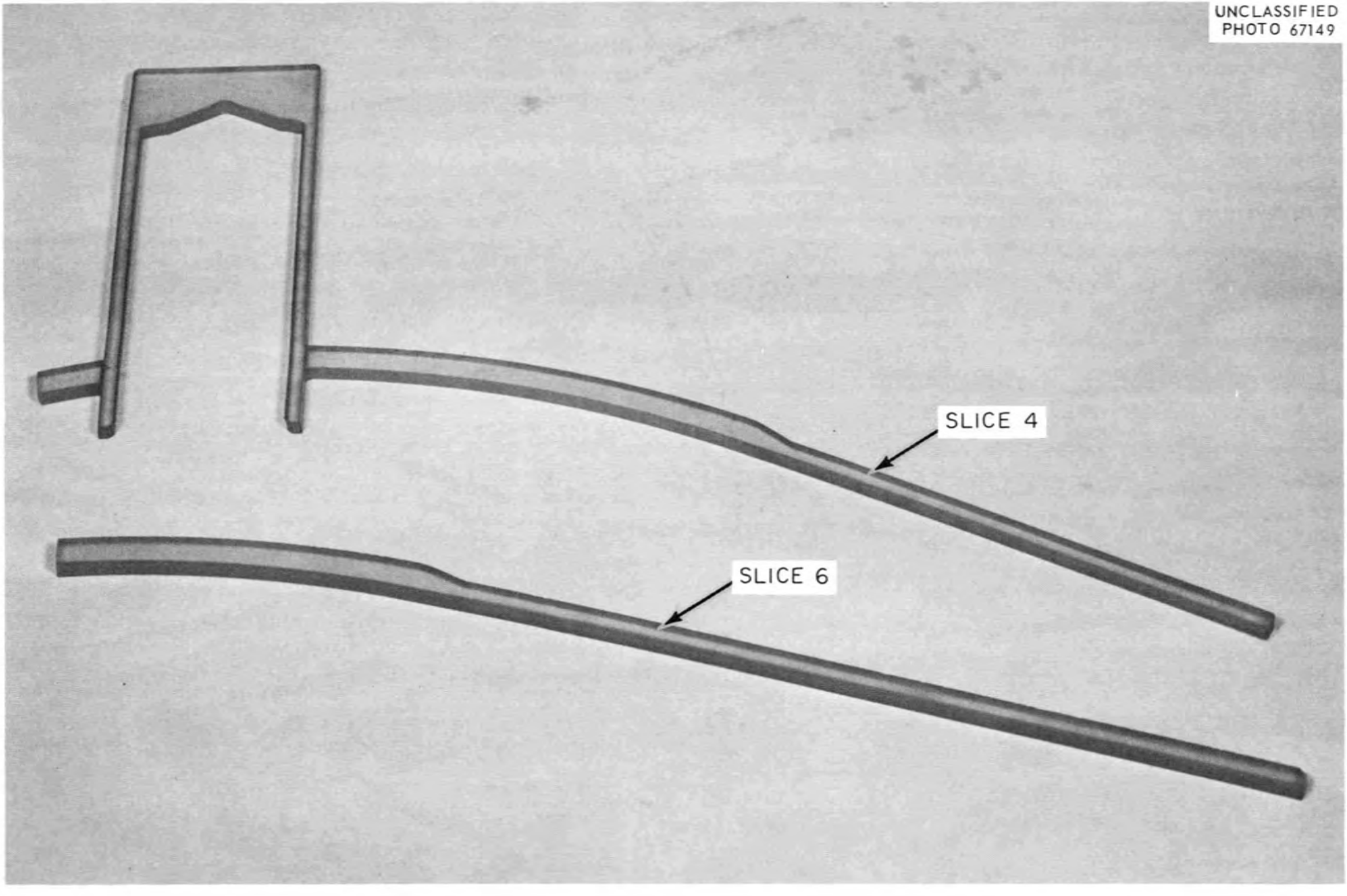

Fig. 9. Slices 4 and 6 Through Head and Shell.

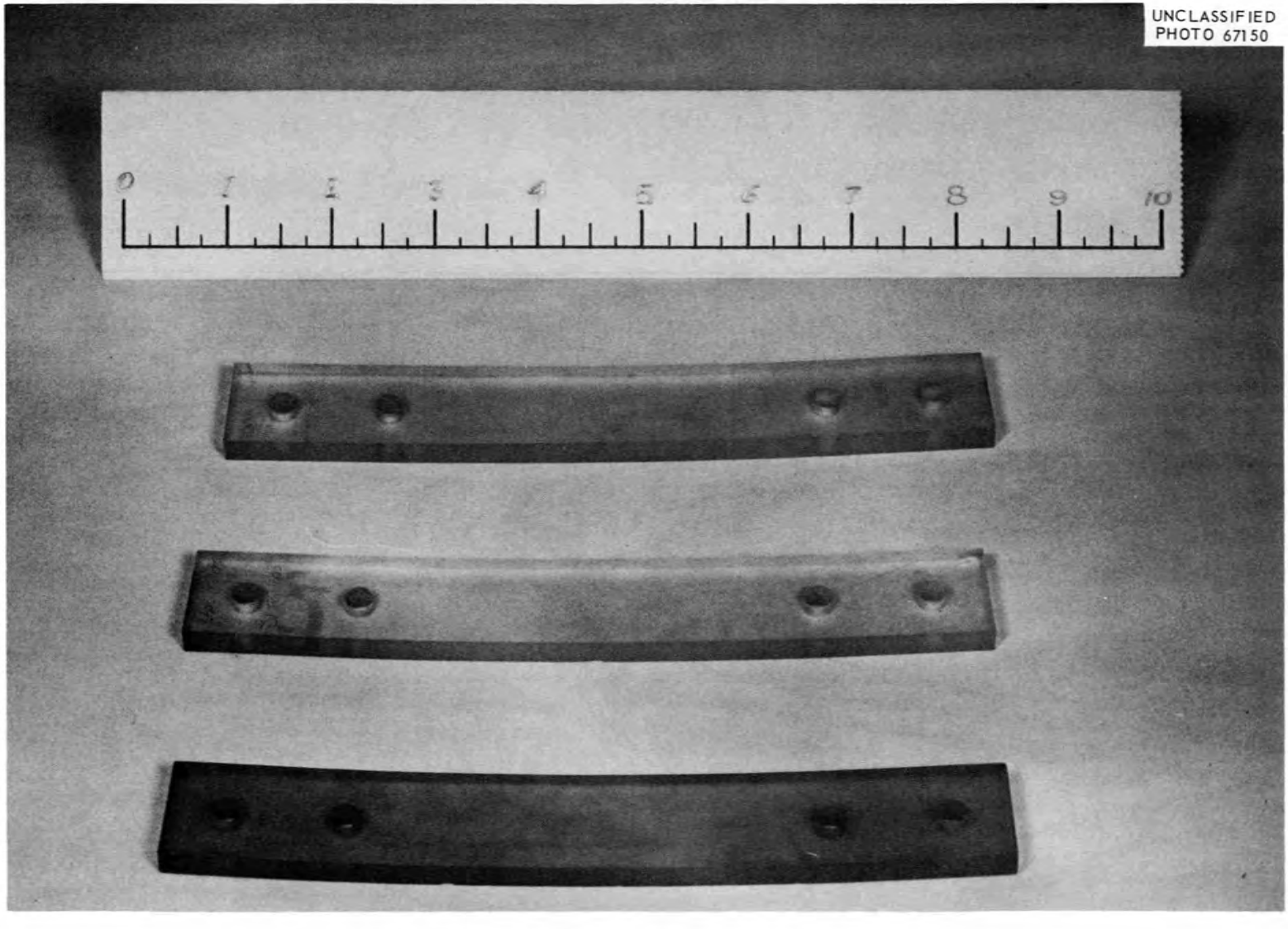

Fig. 10. Calibration Bars After Loading.

negative, the compensator must be placed parallel to the boundary for extinction to occur. The fringe factor for the compensator was determined experimentally, while that for the model was determined from the stress-frozen calibration bars of the same material by the Tardy in-out method[4] for finding fractional fringe orders. The frozen stress patterns in the calibration bars are shown in Fig. 11. These patterns indicated pure bending when removed from the oven. However, some time and edge-effect

[4]M. M. Leven, Quantitative Three Dimensional Photoelasticity, SESA Proceedings, Vol. 12, No. 2, 1954.

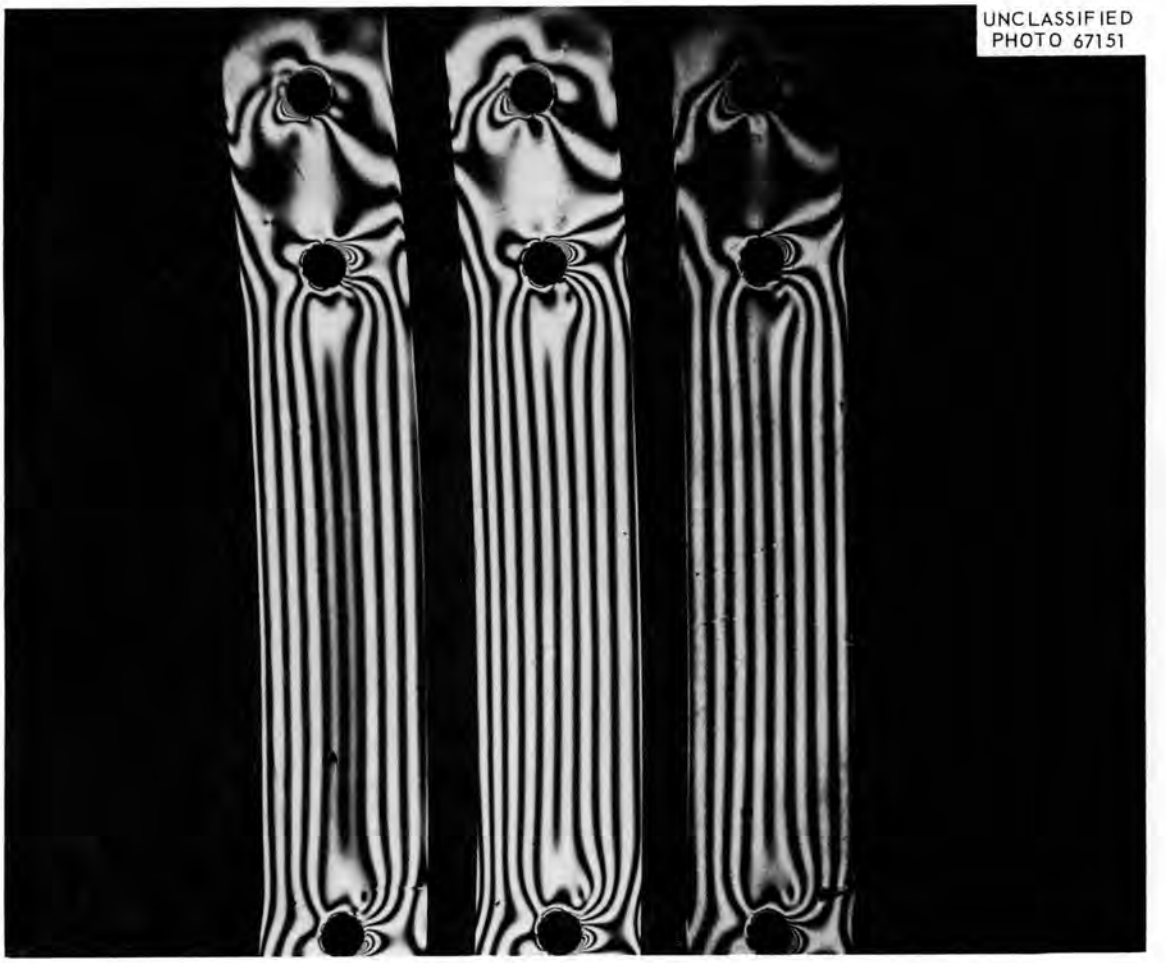

Fig. 11. Frozen Stresses in Calibration Bars.

stresses[5] or time stresses[6] are apparent in the photograph. Steps were taken to minimize time stresses (one week in a desiccator followed by oil-bath storage), but problems were encountered with the thin nozzle sections that precluded obtaining good data in the cluster nozzles and determining the membrane stress in nozzle A. These problems are described in Section 5.

For relating the stresses in the model to prototype stresses, the following relationships[7] were used:

$$\sigma_p = \sigma_m C_1 ,$$

where

$$C_1 = \frac{P_p}{P_m} \qquad \text{or} \qquad C_1 = \frac{f_p/L_p^2}{f_m/L_m^2} ,$$

and

σ_p = stress in prototype,
σ_m = stress in model,
P_p = internal pressure in prototype,
P_m = internal pressure in model,
f_p = concentrated load in prototype,
f_m = concentrated load in model,
L_p = characteristic length of prototype,
L_m = characteristic length of model.

Upon combining the above relationship with the compensator relationship, the prototype surface stresses can be directly determined from

$$(p - q)_p = \frac{(k)(\text{average compensator reading})}{(\text{thickness of the model})} ,$$

where k is an overall constant that depends upon C_1.

---

[5]M. M. Frocht, Photoelasticity, Vol. I, pp. 364–365, Wiley, New York, 1941.

[6]M. M. Frocht, op. cit., Vol. II, pp. 376–381.

[7]B. L. Greenstreet et al., op. cit., pp. 33–34.

The results obtained for the prototype with the use of the above relationships required, in some cases, further modification because of differences in Poisson's ratio. In the case of cylindrical shells (nozzles) subjected to bending by axisymmetrical edge loads, the circumferential bending stresses are directly proportional to Poisson's ratio. This is also true when loads are applied to the outer edge of a hemispherical shell or spherical segment where the included half-angle is approximately 60 deg or greater. (The Geckler approximation, which gives results similar in form to those for cylinders, is applicable for the analysis of these spherical shells.[8]) Thus, where bending stresses are significant, the Poisson's ratio effect must be considered.

In the case of the EGCR vessel, the regions where Poisson's ratio is important are in the nozzles and near the head-to-shell junction. Since the total circumferential stresses on the two surfaces are known and may be divided into the membrane, σ_M, and bending, $\mu\sigma_B$, components,

$$\sigma_\theta = \sigma_M \pm \mu\sigma_B ,$$

the necessary corrections are easily made. Here, μ is Poisson's ratio and σ_B is the bending stress in the axial (or meridional) direction.

The effect of the Poisson's ratio variation in the head and shell was found to be within the scatterband of the experimental points and was thus neglected in these regions. This effect was significant in the nozzles, however, and corrections were incorporated in the nozzle results.

The compensator data were read as the output of a Wheatstone bridge composed of strain gages on a cantilever beam to which the compensator specimen was attached. The bridge output was calibrated to allow conversion of the strain-gage readings to actual stress in the compensator. To obtain stresses in the circumferential direction, the axial and meridional slices were subdivided into small pieces of varied thickness, depending upon the location and the geometry. In general, the dimension of a subslice was 1/16 in. in a direction along the original slice.

---

[8]S. Timoshenko and S. Woinowsky-Krieger, Theory of Plates and Shells, 2nd ed., pp. 547-554, McGraw-Hill, New York, 1959.

In order to determine the stresses due to the combined loads on nozzle M_3, it was necessary to separate the photoelastic effect of the two loading conditions. This was accomplished by subtracting the compensator readings of nozzle M_4, which was subjected to the pressure loading only, from the readings of nozzle M_3 to obtain the birefringent effect of the axial load. Different scaling factors were applied to the separate data, and the resulting stresses were combined by superposition to obtain stresses corresponding to the design loadings of 350 psi internal pressure and 42,000 lb axial nozzle load for the prototype.

The directions of the principal stresses in the head near the hillside nozzles were checked by examining an area surrounding a K nozzle. Isoclinic[9] lines along which the principal stresses had parallel directions were obtained. These were for the 0° and 90° directions and the 45° directions with respect to a meridional line passing through the center of the nozzle. This line was coincident with the major axis of the elliptical intersection between the shell and the nozzle. Figure 12a shows loci of points with principal stresses parallel to the elliptical axes of the nozzle to head intersection. Figure 12b shows the points with principal stresses parallel to planes 45° from the elliptical axes. In the photographs the darkest zones adjacent to the nozzle are isoclinic lines and are different in each picture. The lighter fringes that appear in both photographs are due to membrane stresses. These photographs were overexposed to produce greater contrast of the isoclinic lines. The principal stress directions in the head at the nozzle intersection were parallel and perpendicular to the line of intersection for all planes through the center of the nozzle.

Isoclinic lines were also obtained in a hillside nozzle near the intersection with the head. Figure 13 shows the profile of a hillside nozzle along with a plot of the isoclinic lines and stress trajectories[10] (principal stress directions) on a developed surface of the nozzle from the uphill to the downhill positions (points a and b, respectively). The principal stress directions in the nozzle at the intersection with the head are also shown to be perpendicular and parallel to the line of intersection.

---

[9]M. M. Frocht, op. cit., Vol. I, pp. 177–179.

[10]Ibid., p. 42.

UNCLASSIFIED
PHOTO 67152

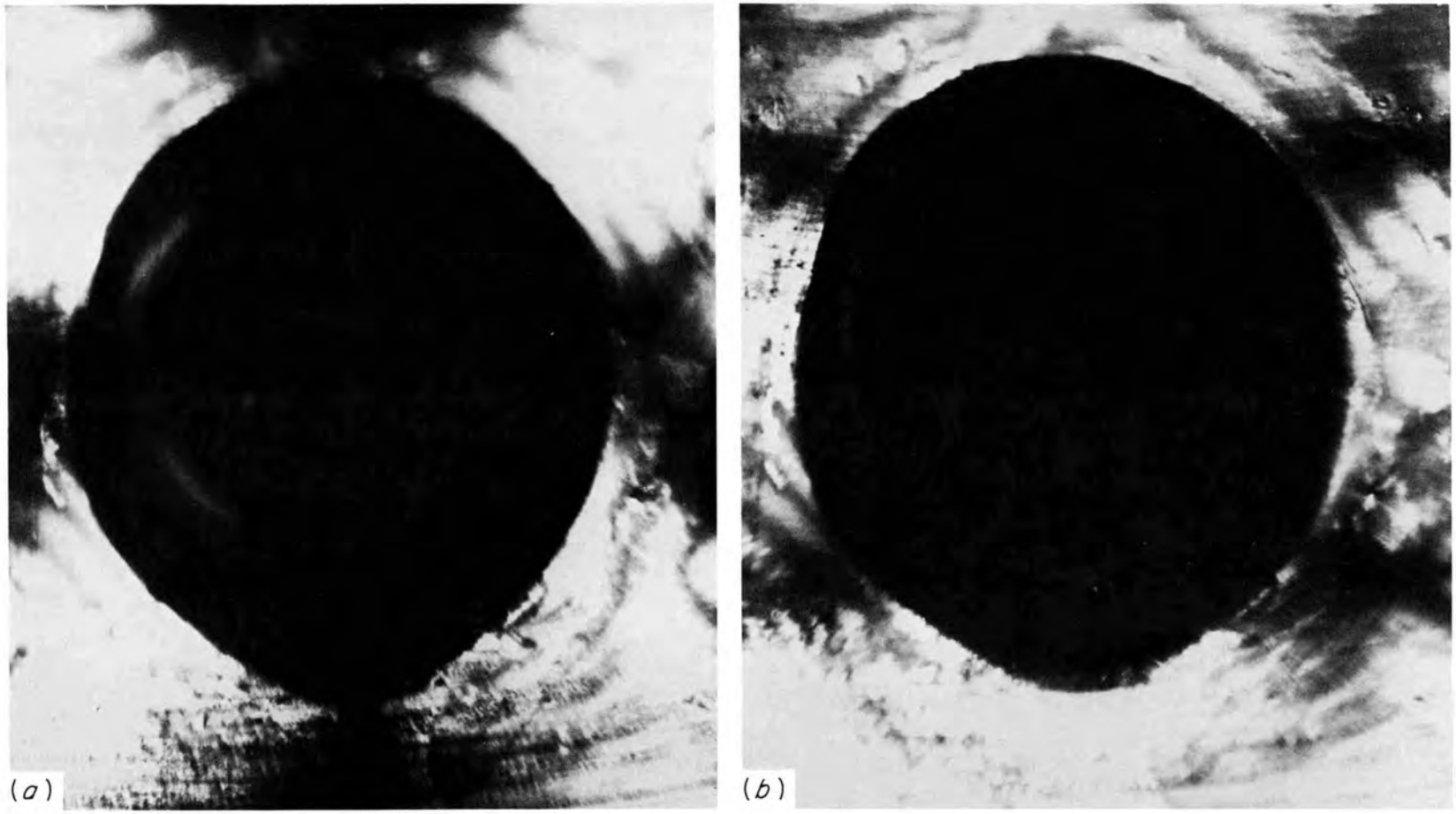

Fig. 12. Isoclinic Lines in the Head Around a Hillside Nozzle.

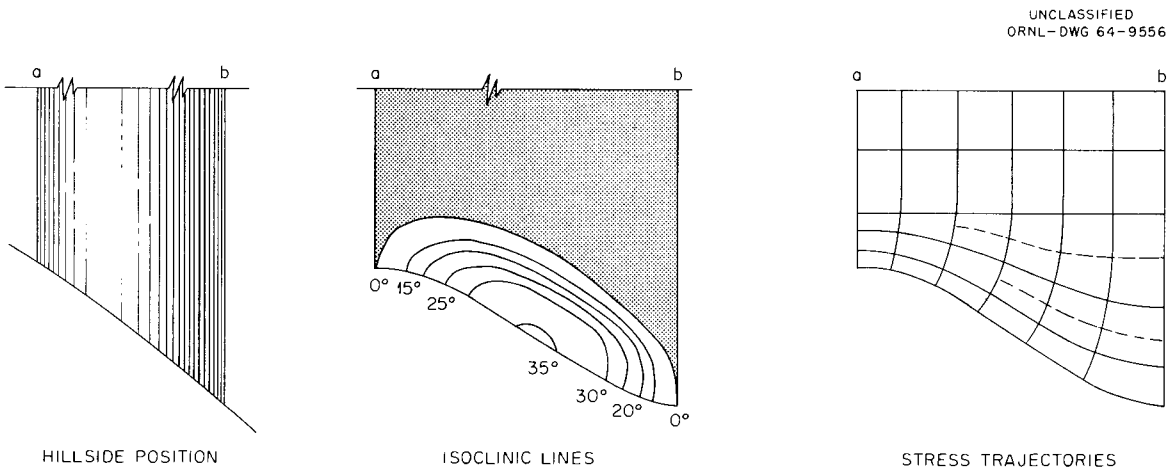

Fig. 13. Isoclinic Lines and Stress Trajectories in a Hillside Nozzle.

4. Results

The results of the tests were scaled to the prototype. These scaled data are shown graphically in Figs. 14 through 35. The pressure stresses obtained from the head and shell regions of the photoelastic model are shown in Figs. 14 through 30 and in Fig. 35. The results from the strain-gage analysis are included in these figures for comparison. The stresses shown in Figs. 27 and 29 for the region adjacent to nozzle M_3 were influenced by the simultaneously applied axial load on nozzle M_3 of 42,000 lb. The strain-gage values shown reflect this axial load. Stresses in the burst-slug-detection (BSD) and gas-outlet nozzles are shown in Figs. 31 through 34.

In Figs. 18 through 30 the broken portions of the circumferential stress curves indicate extrapolations. Due to the slicing arrangement, all circumferential photoelastic points indicate average values. The exact value at the nozzle-head intersection could not be obtained experimentally, as in the case of the meridional or axial stresses. Horizontal lines through strain-gage points indicate the length covered by the strain gages and consequently the length over which each point indicates an average value.

As an aid to the reader, the figures have been indexed as shown in Table 1. This table gives both the figure and page numbers.

Table 1. Arrangement of Figures and Slice Orientation

Region	Slice No.	Pressure Stresses		Combined Stresses	
		Figure	Page	Figure	Page
Head and shell (through BSD nozzle)	1	14–15	27–28		
Head and shell (remote from BSD)	6	16–17	28–29		
Head between nozzles A and B	3	18	29		
Head between nozzles B and D	3	19	30		
Head between nozzles D and G	3	20	30		
Head between nozzles G and K	3	21	31		
Head below nozzle K	3	22	31		
Head between nozzles A and C_3	1	23	32		
Head between nozzles A and C_4	2	24	32		
Head between nozzles C_3 and F_3	1	25	33		
Head between nozzles C_4 and F_4	2	26	33		
Head between nozzles F_3 and M_3	1			27	34
Head between nozzles F_4 and M_4	2	28	34		
Head below nozzle M_3	1			29	35
Head below nozzle M_4	2	30	35		
Burst-slug-detection nozzle					
As taken	4	31	36		
Corrected	4	33	37		
Gas-outlet nozzle					
As taken	1	32	36		
Corrected	1	34	37		
Head adjacent to gas-outlet nozzle	1	35	38		

5. Discussion of Results

Head and Shell Region Below Nozzle Cluster

Stresses were obtained along two meridional planes below the nozzle cluster. One of these planes passed through the burst-slug-detection nozzle (slice 4), while the second was taken at a position remote from any of the large nozzles (slice 6). These data are shown in Figs. 14 through 17 and are compared with strain-gage results obtained along a single plane through the burst-slug-detection nozzle.

The results from the two independent experimental studies show general agreement. An exception may be seen on the outer surfaces of the cylindrical section where the stresses are considerably higher than those obtained from strain gages (see Figs. 14 and 16). Differences are also noted in the circumferential stresses on the inner surfaces near the transition (see Figs. 15 and 17).

Membrane stresses in the spherical shell portion are in good agreement with theoretical values. However, in the region well below the transition from head to shell, the observed circumferential stresses are approximately 20% higher than the theoretical membrane values. The maximum stress, as shown by the photoelastic data, is 19,600 psi and occurs in the circumferential direction (Fig. 14).

The similarity in the photoelastic data taken from the two remote sections may be seen by a comparison of the figures. Since only one of the planes passes through the burst-slug-detection nozzle, it is concluded that the influence of the burst-slug-detection nozzle on the stresses at and below the head-to-shell transition is negligible.

Spherical Head Adjacent to Cluster Nozzles

The head stresses in the cluster region are shown in Figs. 18 through 30. The sections studied are indicated in Fig. 4 as slices 1, 2, and 3. The distributions in the head between nozzles are characteristic of those found in flat perforated plates, with allowances made for the reinforcing effects of the nozzles. These reinforcing effects are more pronounced for the stresses normal to the perforations than those in the tangential direction. As a result, there are increases in the meridional stresses at the edges of the nozzles, where these stresses would be zero for unreinforced perforations. The increase in meridional stress midway between nozzles, as shown in Figs. 20, 25, 26, and 27, also corresponds to perforated plate characteristics.

From these observations, distributions associated with single nozzle-to-shell attachment configurations are not prominent for head regions between the cluster nozzles. Thus, theoretical analyses made using such models could not be expected to yield applicable results. This was borne out by comparisons made by Greenstreet and his co-workers.[2]

In cases where good glued joints were not obtained, the stresses adjacent to the junction and normal to the nozzles should tend toward zero values. This follows from the perforated-plate analogy. An example of this tendency may be seen by comparing the meridional stresses on the outer surfaces that are shown in Figs. 23 and 24.

The stresses in the head around nozzle A obtained from strain gages did not show appreciable variation with angular orientation. More variation was noted from the photoelastic data (Figs. 18, 23, and 24). This is partly attributable to a glued nozzle connection in the plastic model as compared with a more uniform welded and machined connection in the aluminum model. The glued nozzle joints in the model were found, in some cases, to be nonuniform and sometimes very fragile, while in other cases they were found to be very strong. This may have been a contributing factor in the lack of agreement between the photoelastic and strain-gage analyses in this area. Another reason for the observation of more variation in the head stresses around nozzle A was the availability of photoelastic data close to the junction of the nozzle and the head as compared with average values from gages adjacent to the junction.

In comparing the photoelastic stresses between similar nozzles (Figs. 23 through 26), it is observed that with the exceptions mentioned above, there is fairly close agreement in both distribution and magnitude of the stresses. Not all the discrepancies between photoelastic and strain-gage results rest with model fabrication, however. Throughout the cluster region, differences in stresses in areas with high stress gradients are caused by averaging the strains over the length of the gages. (Typical examples would be the meridional stresses in Figs. 19 and 20.)

A comparison may be made between the head stresses in the areas adjacent to nozzles M_3 and M_4 (Figs. 27 through 30). The nozzle M_3 results are for an axial load of 42,000 lb downward combined with the 350 psi internal pressure. It can be seen that the axial compressive load contributed very little to the level of stress in the adjacent head areas. In fact, the variation did not exceed the experimental variation experienced between other similar nozzles without axial loading. This was as expected and concurred with the results from the strain-gage analysis.

The maximum head stress found in the cluster region was on the uphill side of nozzle D. This was a circumferential stress of +18,800 psi on the outer surface of the shell, as shown in Fig. 19. Extrapolating from the curve given, the stress at the junction was approximately 20,000 psi.

The largest head stresses generally occurred on the uphill sides of the hillside nozzles, confirming results of other experimental studies.[11] This trend was only general, however, with exceptions being found in the head around nozzles B, K, and M_4. Lack of data precluded the observation of any such trend in the strain-gage analysis.

Nozzle Stresses

The stresses in the burst-slug-detection and gas-outlet nozzles were found to be uniformly shifted in magnitude from the strain-gage values. This was especially true on the outer surfaces, as shown in Figs. 31 and 32, where exposure to atmospheric influences was greater than on the inner surfaces. The shift was attributable mainly to time stresses, although other factors could have contributed. The curves were adjusted to compensate for these displacements by adding a constant, equal to the difference in magnitude between the measured and theoretical stresses in the membrane region, to the stress values for a given distribution. Since Poisson's ratio for the photoelastic model was 0.48, while the value for the prototype was 0.30, the circumferential stresses in the bending regions, as obtained from the photoelastic model, were modified, as previously discussed (in Sect. 3), to compensate for this difference. The effects upon the stress distributions arising from nozzle weight during the stress-freezing cycle were evaluated and found to be negligible. The adjusted results are shown in Figs. 33 and 34, along with the results for the inner surfaces.

On the outer surfaces, the solid lines are theoretical curves fit to the strain-gage data,[12] while on the inner surfaces the solid lines represent theoretical stresses derived from the outer surface experimental data. The agreement observed between the modified photoelastic distributions and the strain-gage data shows that consistent results were obtained from the two independent tests. This agreement becomes even more significant when it is remembered that any inaccuracies or differences were magnified by the

---

[11] R. T. Rose et al., Stresses at Oblique Nozzles in Spherical Pressure Vessels, Symposium on Pressure Vessel Research Towards Better Design, London, January 18–19, 1961, Institute of Mechanical Engineers.

[12] B. L. Greenstreet et al., op. cit., pp. 35–39.

scaling factors on both pressure and size, and these factors were greatly different for each model.

The stresses at the burst-slug-detection nozzle-to-head junction obtained from the photoelastic study are in good agreement with those obtained from the strain-gage analysis, with one exception. Major differences were found between the axial stresses on the outer surface of the nozzle immediately adjacent to the head. The observed agreement in all respects other than this notable exception makes it apparent that the values in this region obtained by photoelasticity were not indicative of the axial stress in the junction region on the outer surface of the nozzle. (This reduction in axial stress was also observed in the cluster nozzles when a nozzle was not adequately joined to the shell.) The probable edge stress was calculated from the other photoelastic data and the predicted distribution is shown.

From the consistent results obtained for these two nozzles, the accuracy of the experimental data is shown to be high. In addition, the "stress-fitting" technique[12] of using derived curves for extrapolating strain-gage results is verified by the photoelastic study.

Head Adjacent to Gas-Outlet Nozzle

The photoelastic stresses in the spherical head on the uphill side of the gas-outlet nozzle were also found to be displaced. The stresses were adjusted in a manner similar to that for the burst-slug-detection and gas-outlet nozzle data so that the curves passed through the strain-gage data points in the region where the stresses approached theoretical membrane values (Fig. 35). The close agreement between strain-gage data and photoelastic data in the region close to the nozzle justifies the uniform shift in magnitude and gives an indication of the distribution of stresses between and near the strain-gage points.

For comparison, the dotted lines were obtained by fitting the outside circumferential and meridional stresses obtained from the strain-gage model using a technique similar to that applied to cylinders. The stresses fitted were those nearest the junction. In this case the theoretical

expressions for stresses in a thin axisymmetrically loaded sphere were applied.[13]

Stress Directions

The isoclinic lines shown in Fig. 12 verify that in the shell adjacent to the major and minor axes of the ellipse at the intersection of a non-radially attached or hillside nozzle and a spherical shell, the directions of the principal stresses lie parallel to the circumferential and meridional planes of the sphere. In the work of others[11] the directions of the principal stresses were found to be different from the meridional and circumferential stresses. However, the data were taken with strain-gage rosettes mounted at distances clear of the weld fillets where the stress trajectories may have deviated from these directions.

Summary

The maximum head stresses cited in this report are higher than those determined in the strain-gage study. However, even with the approximate extrapolated values, none were as high as the nozzle stress of +21,600 psi obtained from the strain-gage data. The results of the photoelastic analysis verify the conclusions regarding the structural integrity of the prototype set forth in the previous study.[14] The most significant of these is that the design of the upper head of the pressure vessel is adequate for the design loading conditions.

Acknowledgments

This study was initiated by the Engineering Experiment Station, University of Tennessee, under Subcontract No. 875. The model was fabricated and prepared for analysis by the University of Tennessee Department of Mechanical and Aerospace Engineering.

---

[13]F. A. Leckie, Asymptotic Solutions for the Spherical Shell Subjected to Axially Symmetric Loading, Nuclear Reactor Containment Buildings and Pressure Vessels, Butterworth, London, 1960.

[14]B. L. Greenstreet et al., op. cit., p. 81.

The authors wish to acknowledge the aid and assistance of Professors R. L. Maxwell and R. W. Holland of the University of Tennessee in preparing the model. Appreciation is also extended to H. D. Curtis, Senior Engineering Technician, ORNL, who obtained and recorded data.

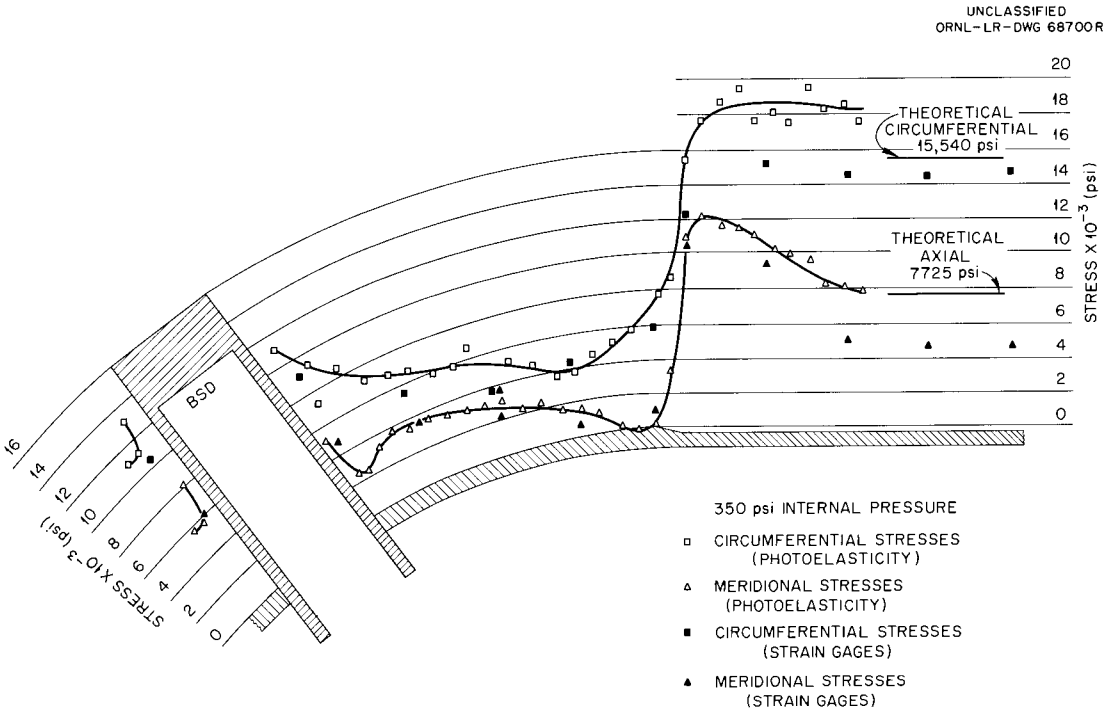

Fig. 14. Stress Distributions on Outer Surfaces of Head and Shell on a Diametral Section Through Burst-Slug-Detection Nozzle.

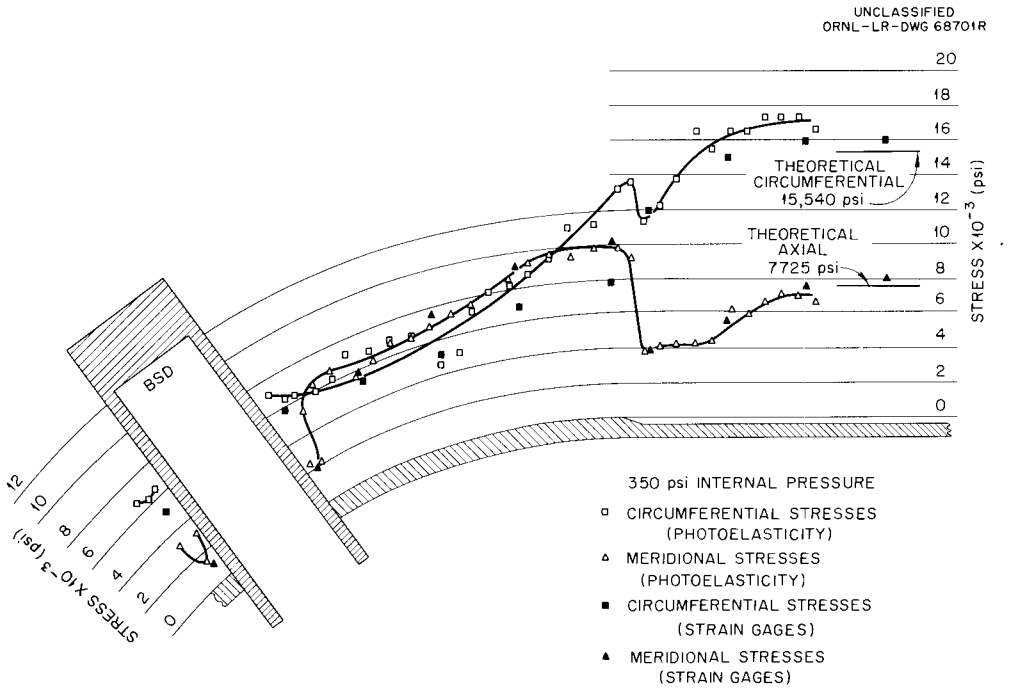

Fig. 15. Stress Distributions on Inner Surfaces of Head and Shell on a Diametral Section Through Burst-Slug-Detection Nozzle.

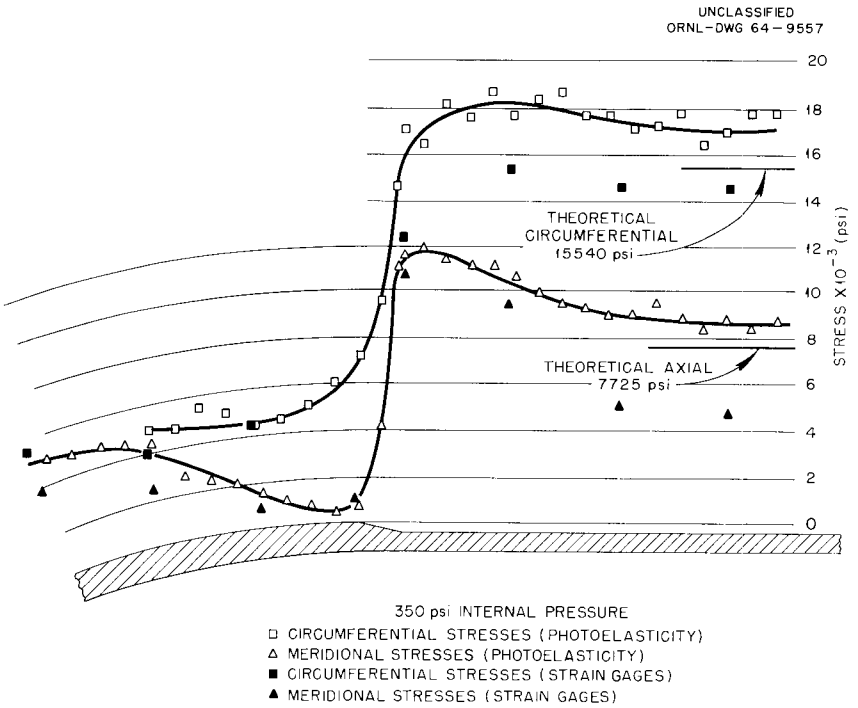

Fig. 16. Stress Distributions on Outer Surfaces of Head and Shell on a Plane Remote from Gas-Outlet and Burst-Slug-Detection Nozzles.

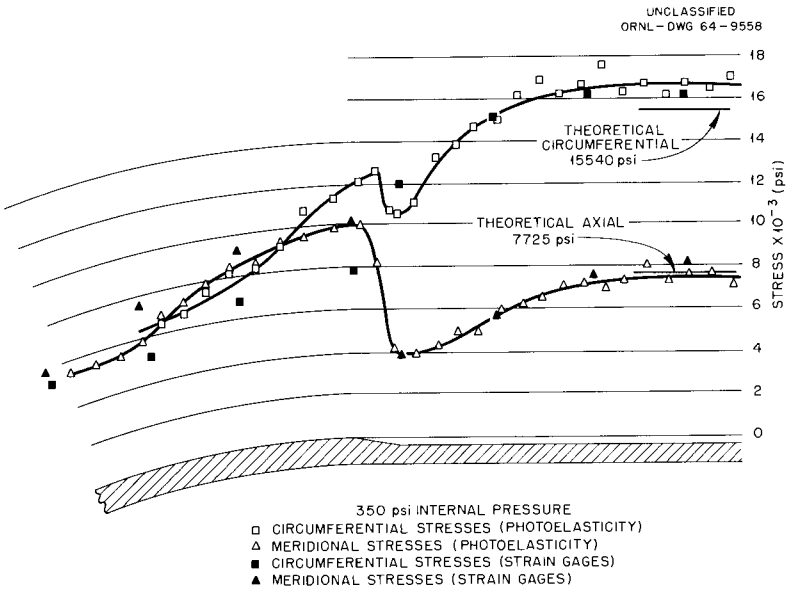

Fig. 17. Stress Distributions on Inner Surfaces of Head and Shell on a Plane Remote from Gas-Outlet and Burst-Slug-Detection Nozzles.

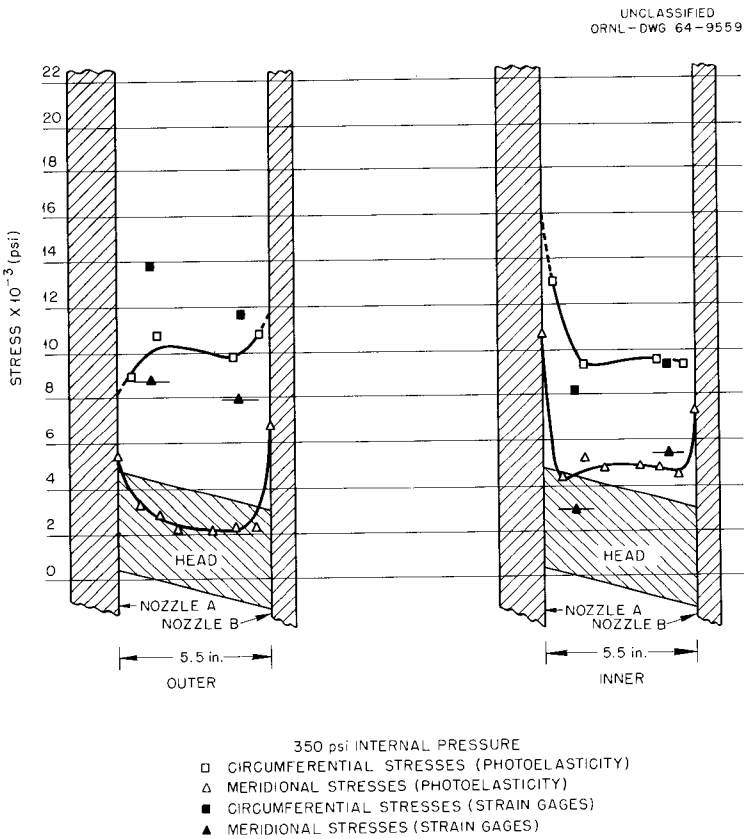

Fig. 18. Stress Distributions on Surfaces of Head Between Nozzles A and B.

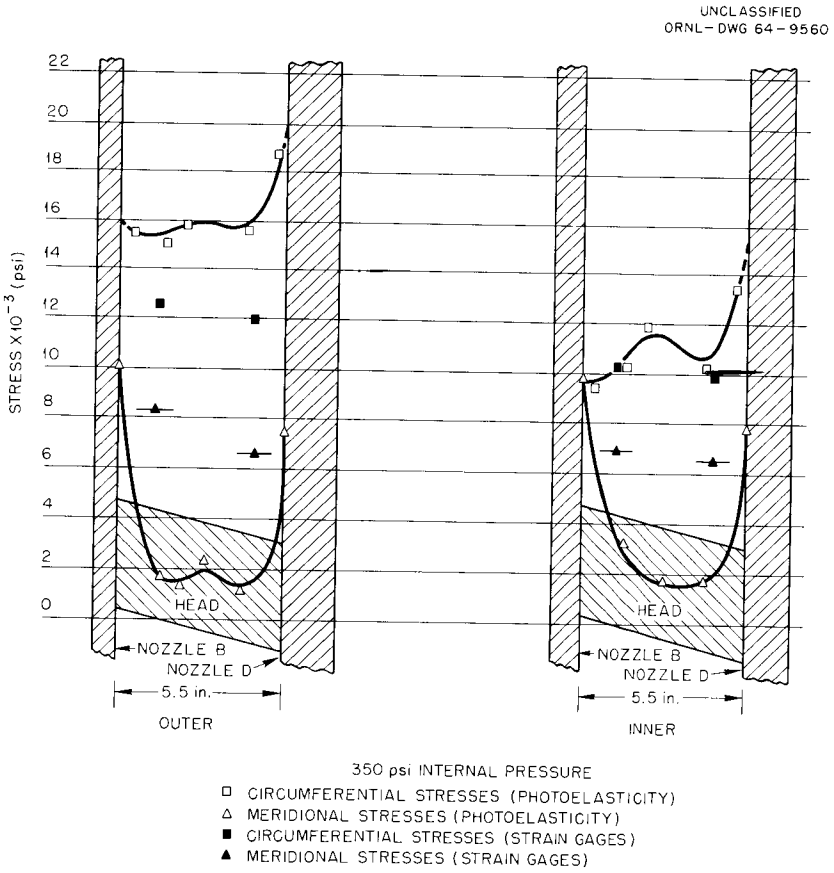

Fig. 19. Stress Distributions on Surfaces of Head Between Nozzles B and D.

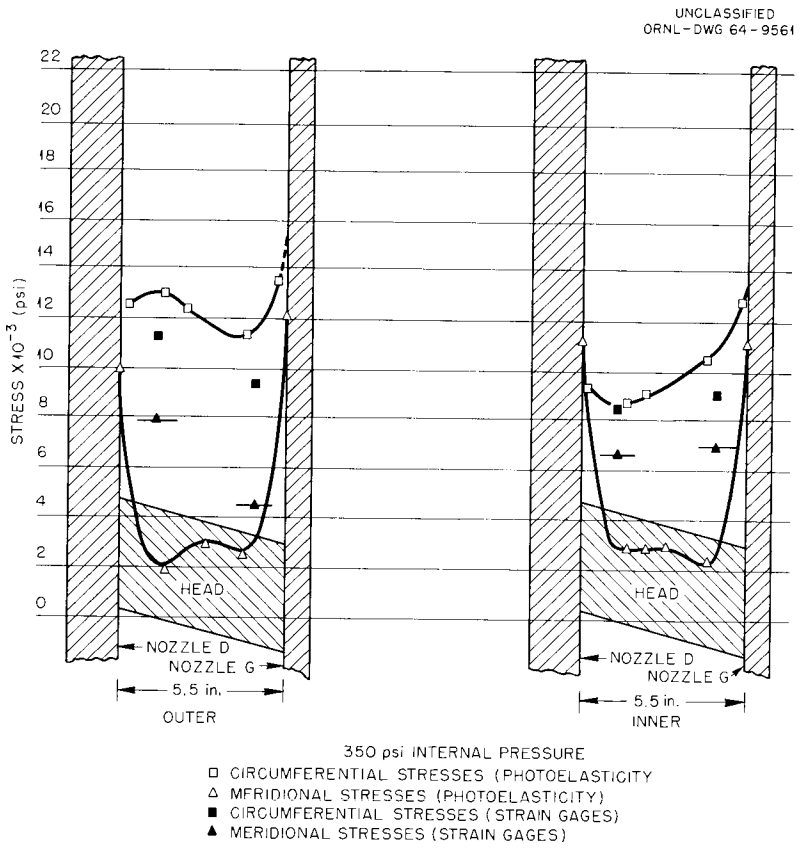

Fig. 20. Stress Distributions on Surfaces of Head Between Nozzles D and G.

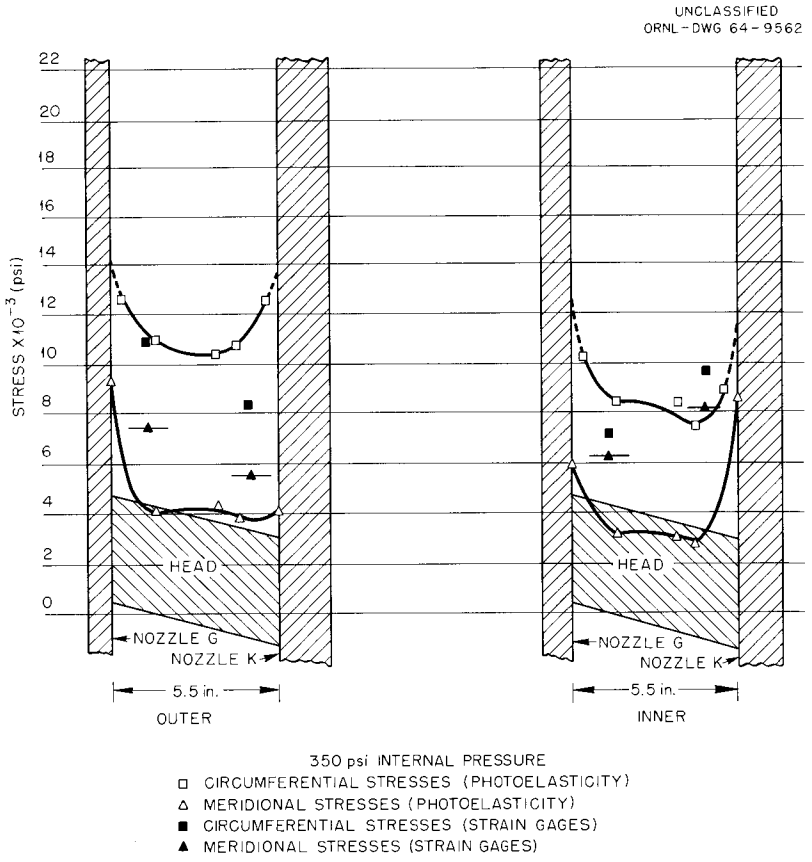

Fig. 21. Stress Distributions on Surfaces of Head Between Nozzles G and K.

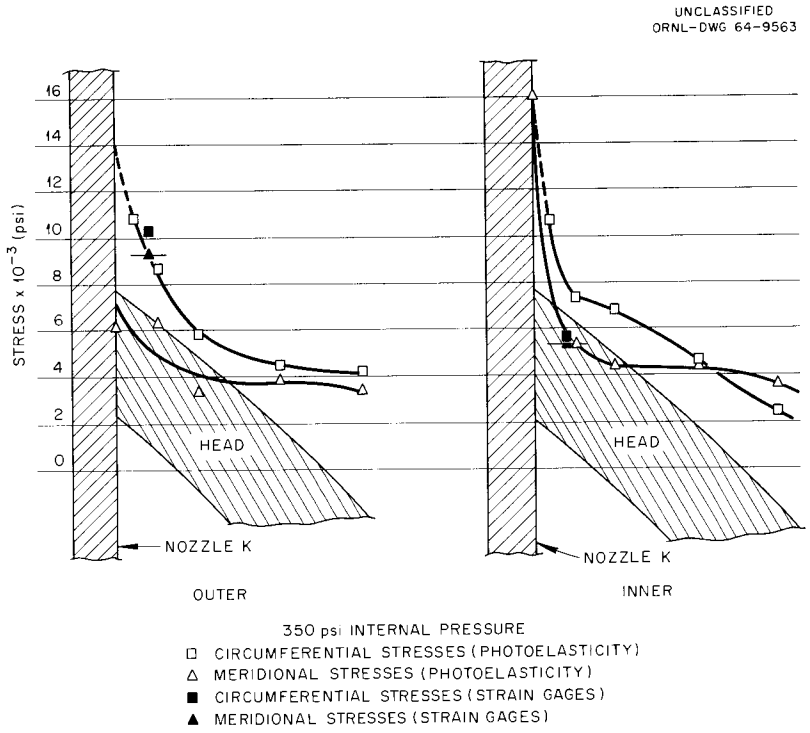

Fig. 22. Stress Distributions on Surfaces of Head Below Nozzle K.

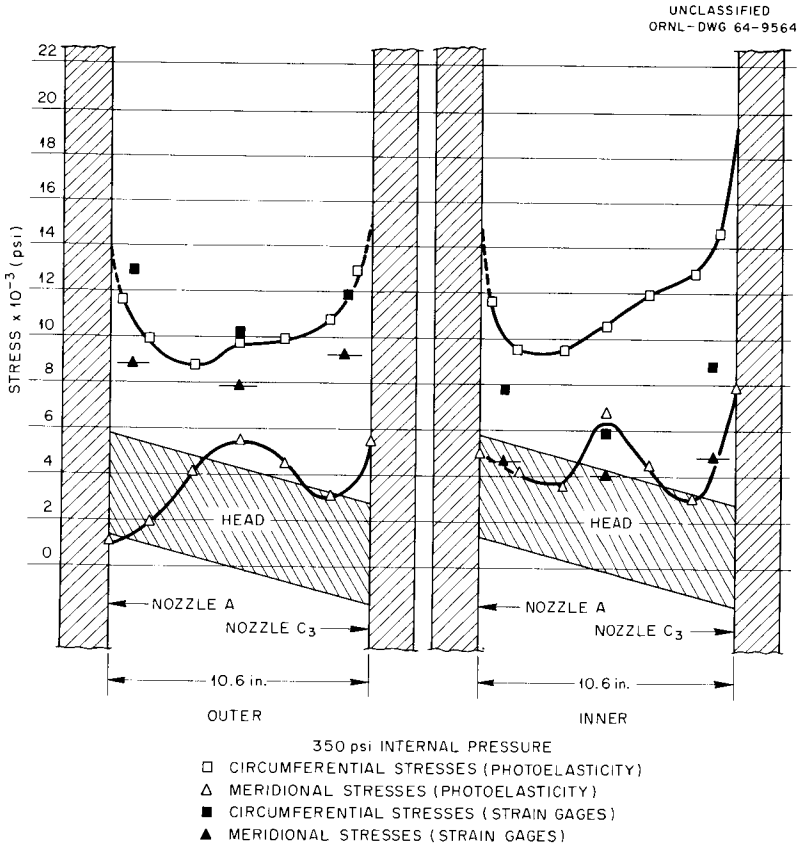

Fig. 23. Stress Distributions on Surfaces of Head Between Nozzles A and C_3.

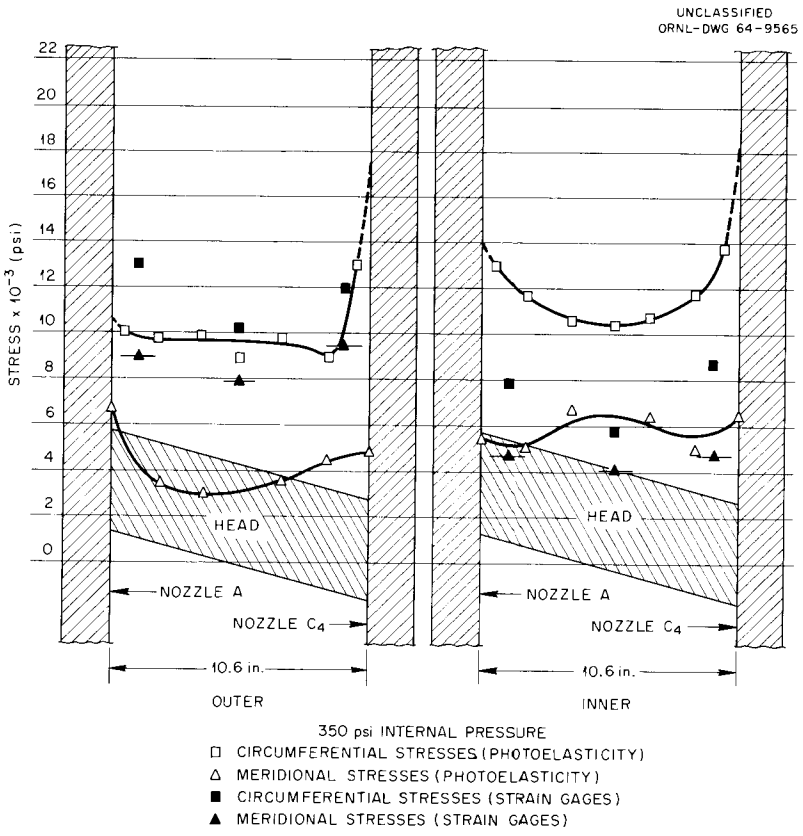

Fig. 24. Stress Distributions on Surfaces of Head Between Nozzles A and C_4.

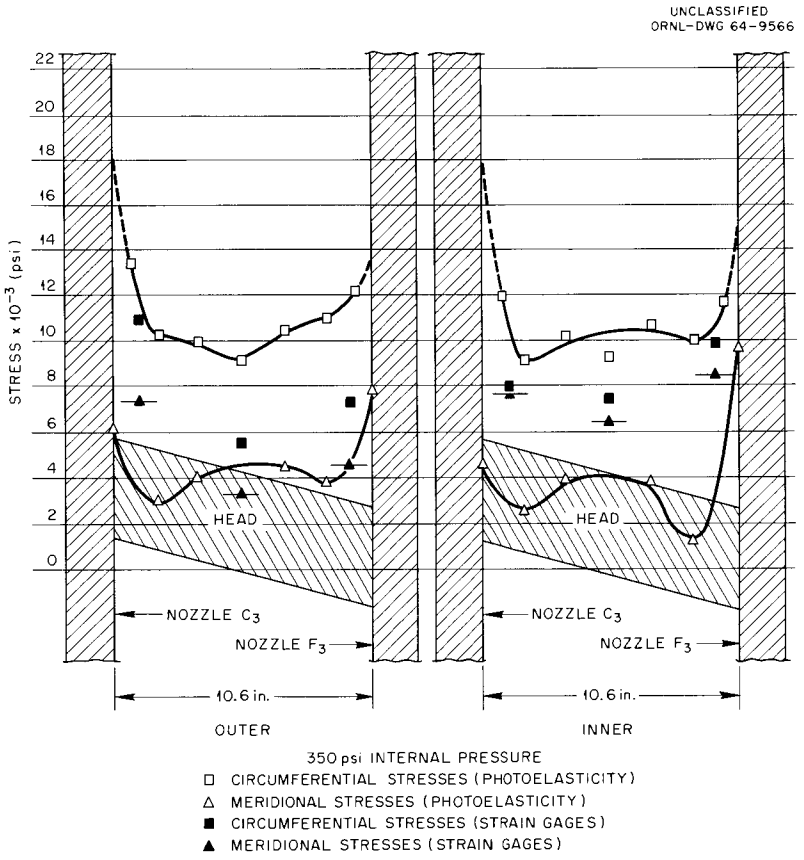

Fig. 25. Stress Distributions on Surfaces of Head Between Nozzles C_3 and F_3.

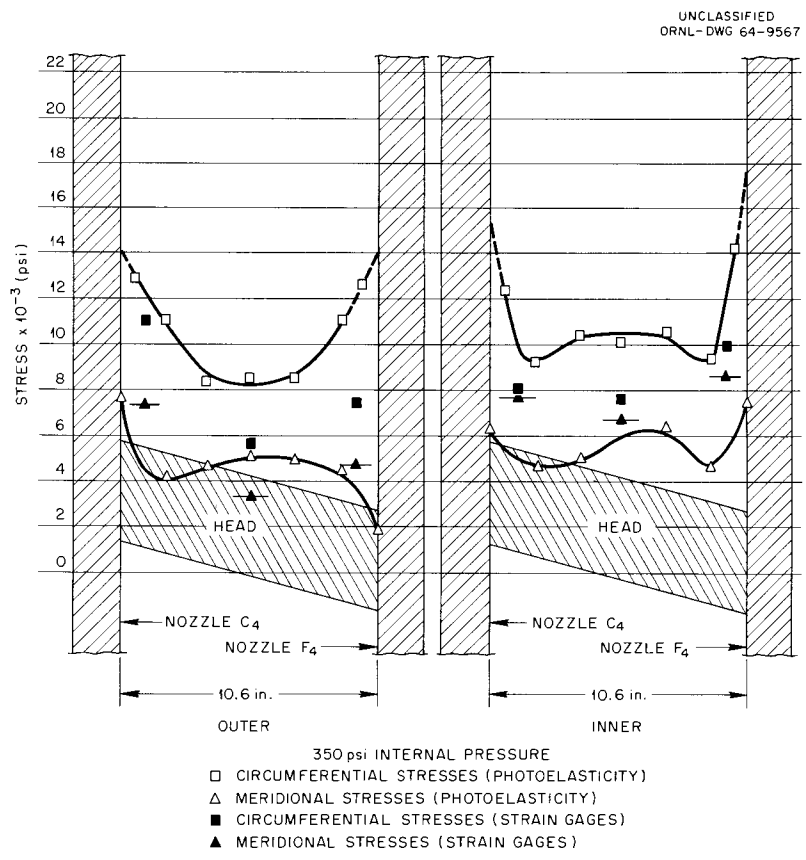

Fig. 26. Stress Distributions on Surfaces of Head Between Nozzles C_4 and F_4.

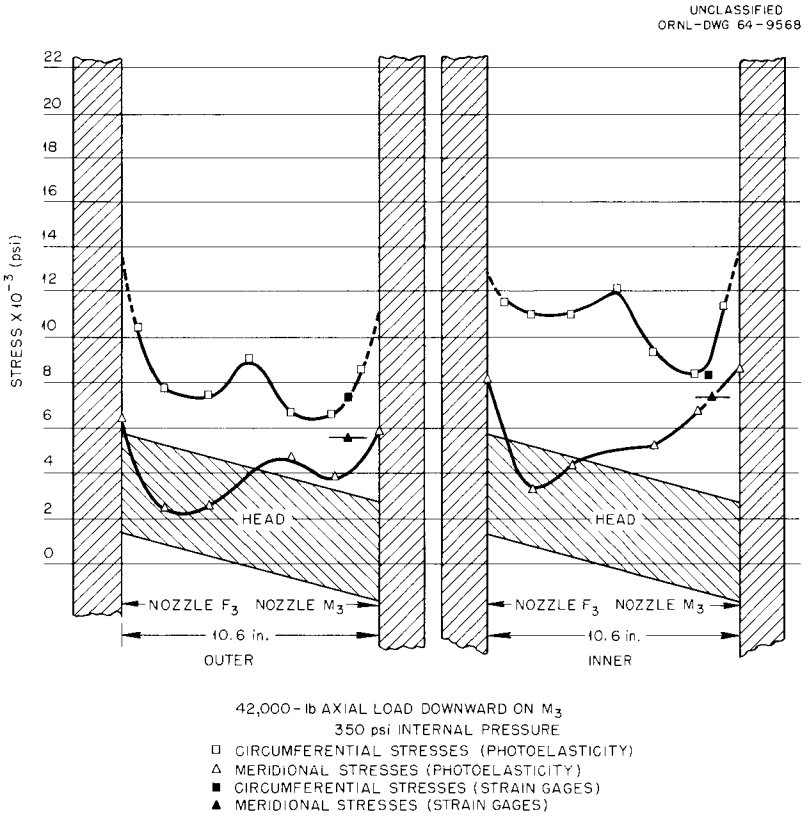

Fig. 27. Stress Distributions on Surfaces of Head Between Nozzles F_3 and M_3.

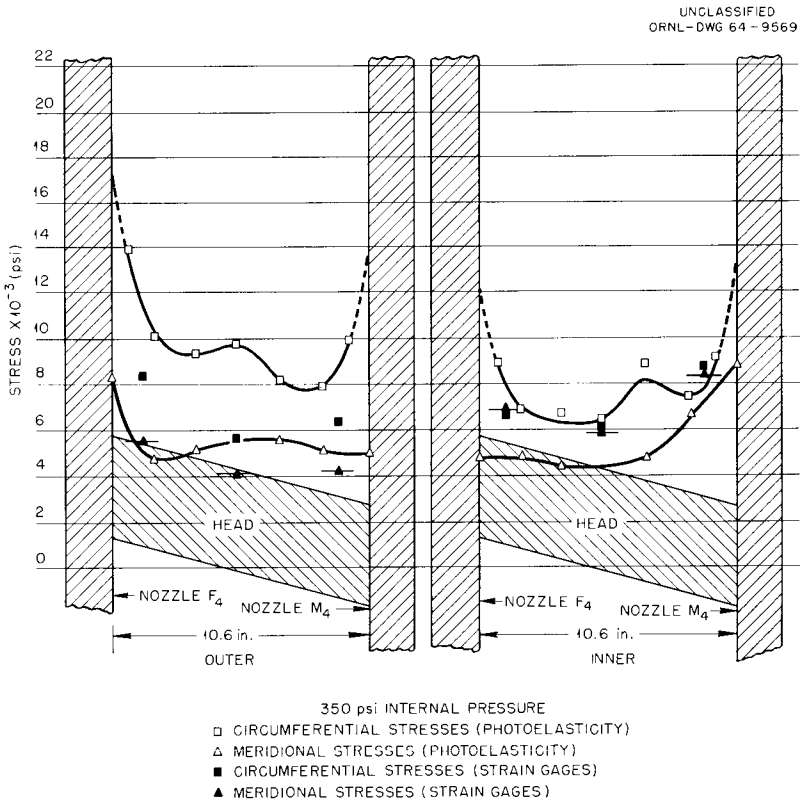

Fig. 28. Stress Distributions on Surfaces of Head Between Nozzles F_4 and M_4.

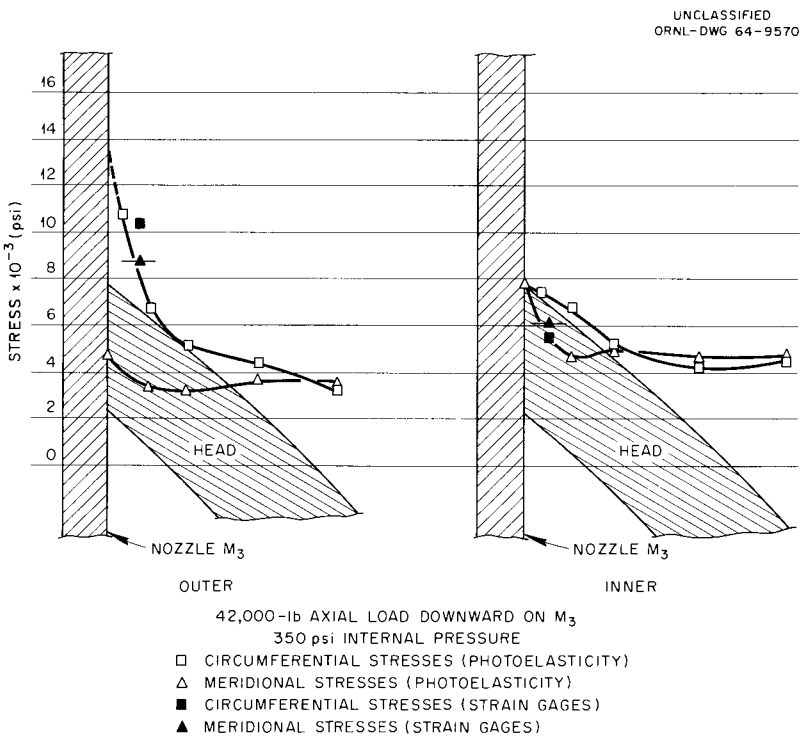

Fig. 29. Stress Distributions on Surfaces of Head Below Nozzle M_3.

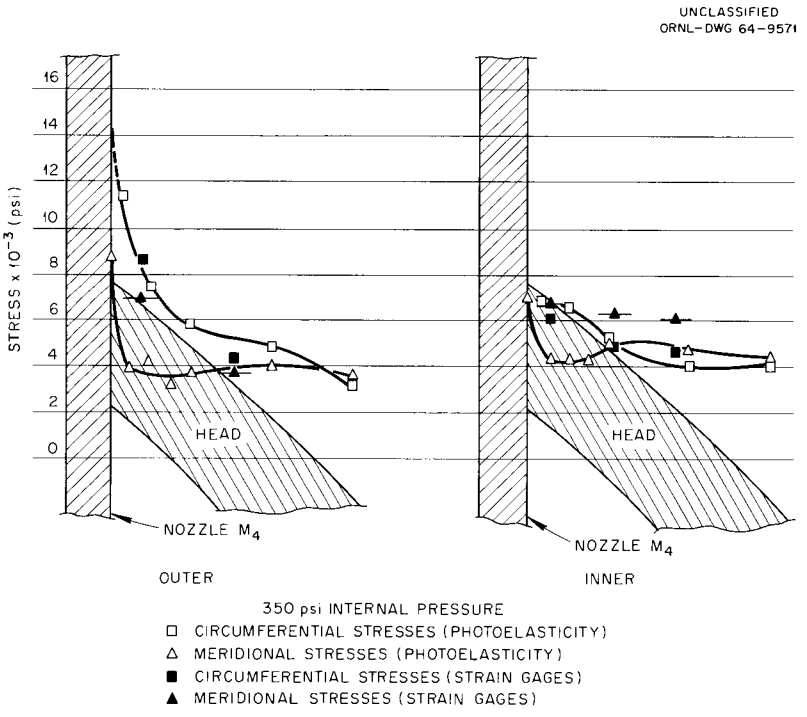

Fig. 30. Stress Distributions on Surfaces of Head Below Nozzle M_4.

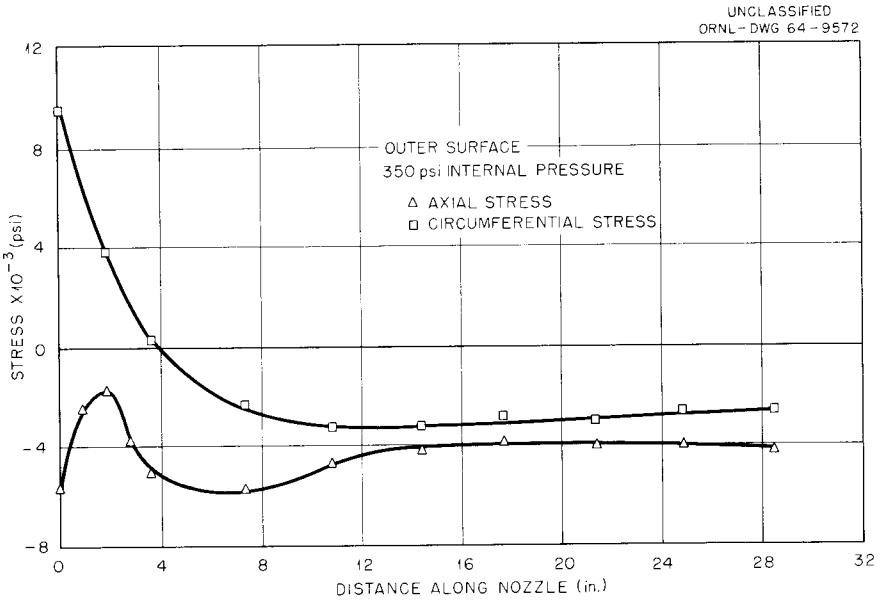

Fig. 31. Stress Distributions on Outer Surface of Burst-Slug-Detection Nozzle Before Correction.

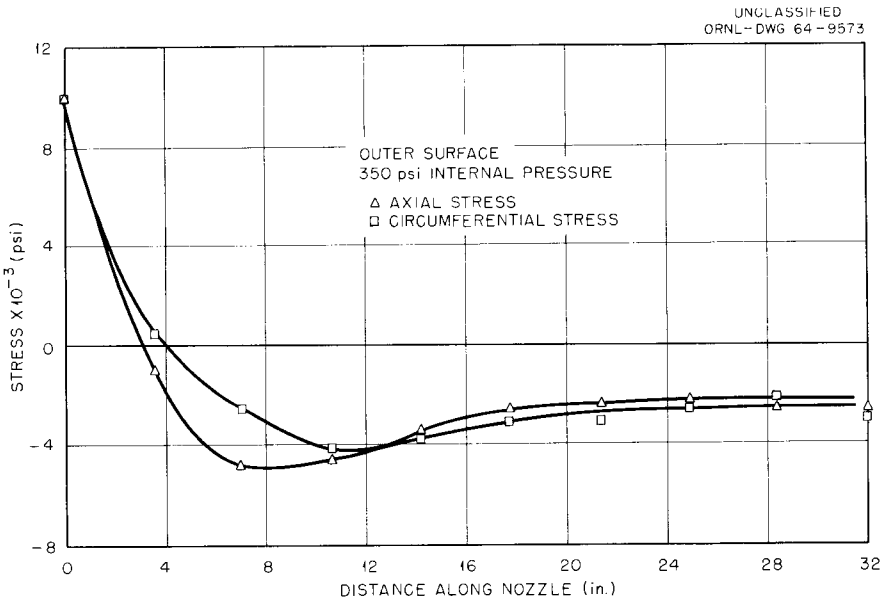

Fig. 32. Stress Distributions on Inner Surface of Gas-Outlet Nozzle Before Correction.

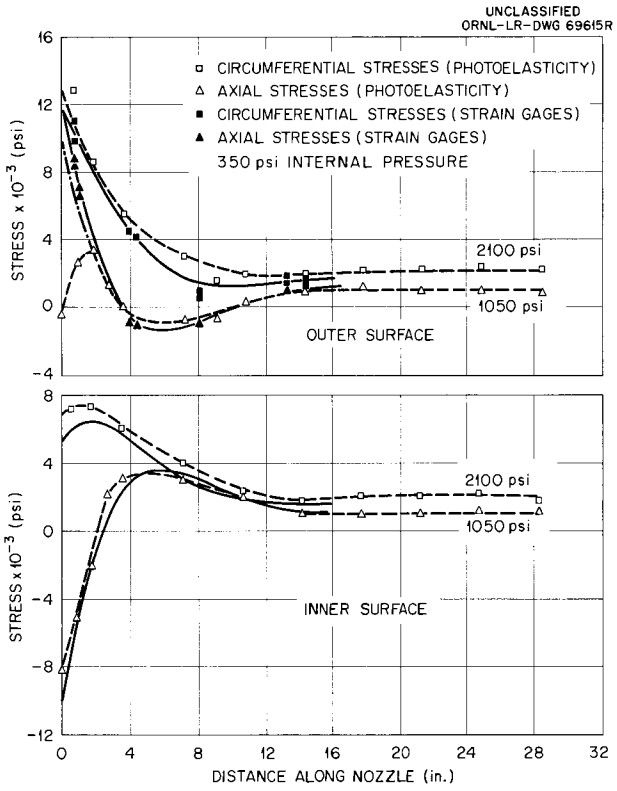

Fig. 33. Corrected Stress Distributions on Surfaces of Burst-Slug-Detection Nozzle.

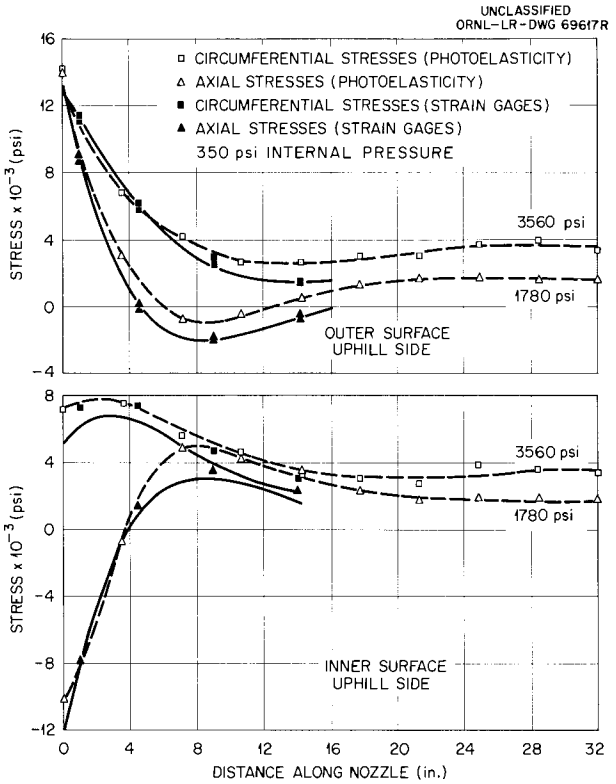

Fig. 34. Corrected Stress Distributions on Surfaces of Gas-Outlet Nozzle.

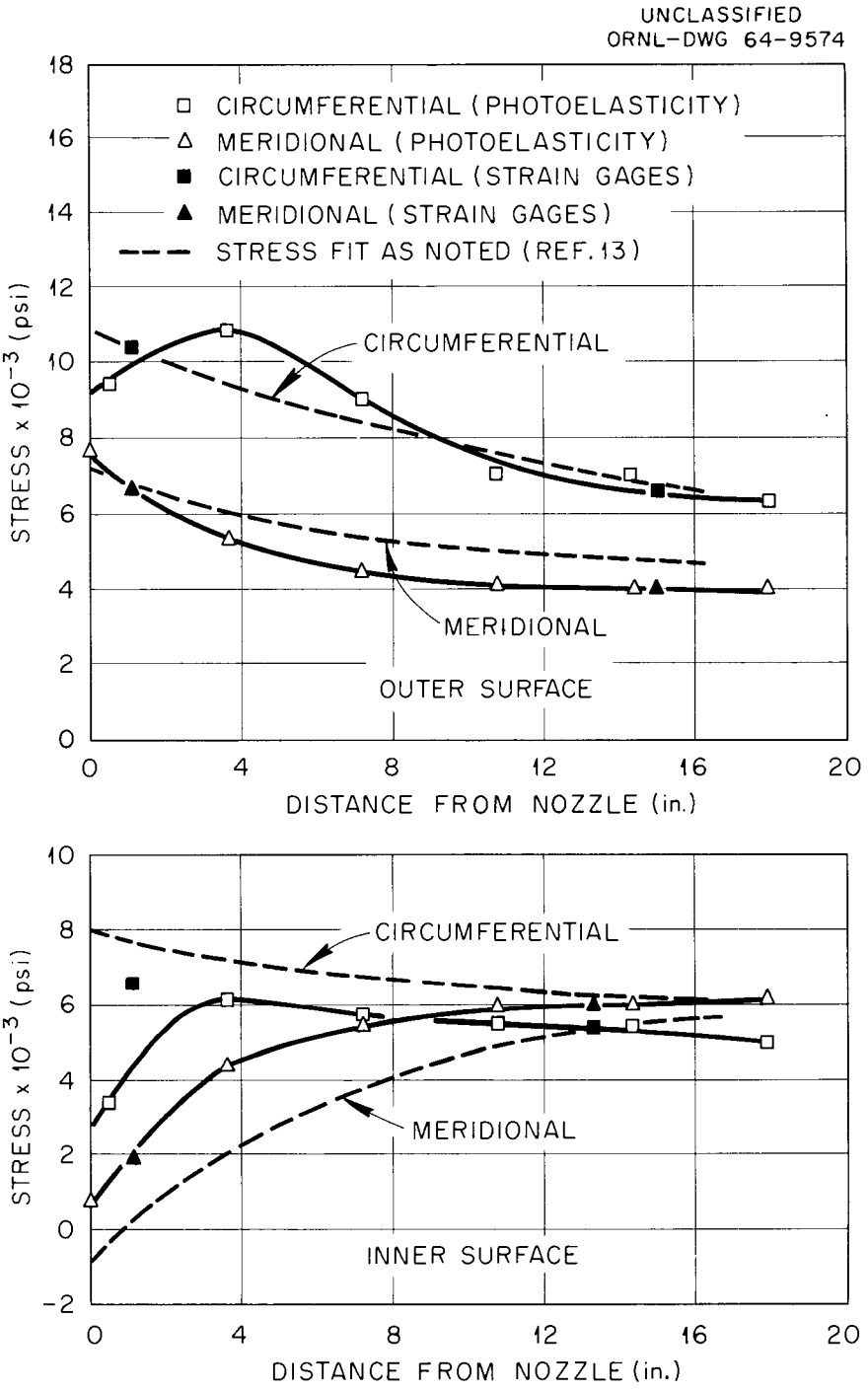

Fig. 35. Stress Distributions on Surfaces of Head Adjacent to Gas-Outlet Nozzle.

ORNL-3690
UC-80 – Reactor Technology
TID-4500 (37th ed.)

Internal Distribution

1. S. E. Beall
2. C. E. Bettis
3. R. E. Biggers
4. C. E. Center (K-25)
5. J. M. Corum
6. W. F. Ferguson
7. W. R. Gall
8–11. B. L. Greenstreet
12. W. F. Johnson
13. C. E. Larson (K-25)
14. M. E. LaVerne
15. R. N. Lyon
16. H. G. MacPherson
17. E. C. Miller
18. S. E. Moore
19. A. W. Savolainen
20. R. W. Schneider
21–35. J. E. Smith
36–73. D. B. Trauger
74. J. T. Venard
75. A. M. Weinberg
76. R. L. Wesley
77–96. G. D. Whitman
97. R. E. Whitt
98–117. F. J. Witt
118. G. T. Yahr
119. F. C. Zapp
120–121. Central Research Library
122–123. Document Reference Section
124–128. Laboratory Records Department
129. Laboratory Records, RC

External Distribution

130. J. F. Bailey, University of Tennessee, Knoxville, Tennessee
131. E. O. Bergman, National Engineering Science Co., Pasadena, California
132. C. W. Brown, University of Tennessee, Knoxville, Tennessee
133. P. D. Bush, Kaiser Engineers, Oakland, California
134. D. R. Carver, Louisiana State University, Baton Rouge, Louisiana
135. A. I. Chalfant, Pratt and Whitney Aircraft, Hartford, Connecticut
136–137. D. F. Cope, AEC, ORO
138. W. E. Crowe, Los Alamos Scientific Laboratory
139. R. M. Evan-Iwanowski, Syracuse University, Syracuse, New York
140. C. Fisher, University of Tennessee, Knoxville, Tennessee
141. A. T. Granger, University of Tennessee, Knoxville, Tennessee
142–147. R. W. Holland, University of Tennessee, Knoxville, Tennessee
148. L. H. Jackson, AEC, ORO
149. B. F. Langer, Bettis Plant, Westinghouse, Pittsburgh, Pennsylvania
150. J. D. Lubahn, Colorado School of Mines, Golden, Colorado
151–156. R. L. Maxwell, University of Tennessee, Knoxville, Tennessee
157. R. V. Meghreblian, Jet Propulsion Laboratory, Pasadena, California
158. J. L. Mershon, AEC, Washington
159. R. L. Miller, Kaiser Engineers, Oakland, California
160. M. Milligan, University of Tennessee, Knoxville, Tennessee

161. W. A. Shaw, Auburn, University, Auburn, Alabama
162. L. R. Shobe, University of Tennessee, Knoxville, Tennessee
163. H. Lawrence Snider, Lockheed Aircraft Corporation, Marietta, Georgia
164–171. W. F. Swinson, Auburn University, Auburn, Alabama
172. K. N. Tong, Syracuse University, Syracuse, New York
173–180. C. C. Wilson, IBM, Lexington, Kentucky
181. Division of Research and Development, AEC, ORO
182–798. Given distribution as shown in TID-4500 (37th ed.) under Reactor Technology Category (75 copies – CFSTI)